

Targeting PLK1-CBX8-GPX4 axis overcomes BRAF/EGFR inhibitor resistance in BRAFV600E colorectal cancer via ferroptosis

Received: 1 May 2024

Accepted: 9 April 2025

Published online: 16 April 2025



Zhan Zhao^{1,8}, Jiashuai He^{1,8}, Shenghui Qiu^{1,2,8}, Lu Wang^{3,8}, Shuchen Huangfu^{1,8}, Yangzhi Hu⁴, Qing Wu⁵, Yabing Yang¹, Xiaobo Li⁶, Maohua Huang⁶, Shijin Liu¹, Hanyang Guan¹, Zuyang Chen¹, Xiangwei Zhang¹, Yiran Zhang¹, Hui Ding¹, Xiaoxu Zhao¹, Guandi Xiao⁷, Yunlong Pan¹, Tongzheng Liu¹✉, Yanping Wu⁷✉ & Jinghua Pan¹✉

Metastatic BRAF^{V600E} colorectal cancer (CRC) confers poor prognosis and represents a therapeutic bottleneck. To identify resistance mechanisms of the mitogen-activated protein kinase (MAPK) pathway in BRAF^{V600E} CRC, we perform genome-wide CRISPR-Cas9 screening and discover that targeting glutathione peroxidase 4 (GPX4) overcomes resistance to BRAF inhibitor (BRAFi) combined with or without epidermal growth factor receptor inhibitor (EGFRi) in BRAF^{V600E} CRC. Specifically, BRAFi ± EGFRi upregulates GPX4 expression, which antagonizes therapy-induced ferroptosis. Moreover, polo-like kinase 1 (PLK1) substrate activation promotes PLK1 translocation to the nucleus, activating chromobox protein homolog 8 (CBX8) phosphorylation at Ser265 to drives *GPX4* expression. Targeting PLK1 enhances BRAFi ± EGFRi inhibition and triggers ferroptosis in vitro, *vivo*, organoid, and patient-derived xenograft model. Collectively, we demonstrate a PLK1–CBX8–GPX4 signaling axis that relays the ferroptosis mechanism of therapeutic resistance and propose a clinically actionable strategy to overcome BRAFi ± EGFRi resistance in BRAF^{V600E} CRC.

Colorectal cancer (CRC) is one of the leading causes of cancer-related deaths worldwide¹. The incidence rate of v-Raf murine sarcoma viral oncogene homolog B1 (*BRAF*) mutation is between 8% and 15% in metastatic CRC (mCRC)², among which BRAF^{V600E} mutation is one of the most common, particularly in right-sided colon cancer³. However, the prognosis of patients with mCRC carrying the BRAF^{V600E} mutation is significantly poor⁴. This mutation

leads to the spontaneous activation of BRAF protein kinase, consequently triggering MAPK signaling pathway. Thus, the proliferation and metastasis of CRC are promoted, leading to poor prognosis in patients with mCRC⁵. Hence, it is imperative to investigate the role and resistance mechanisms associated with the BRAF^{V600E} mutation in CRC to improve the clinical prognosis of patients with BRAF^{V600E} CRC.

¹Department of General Surgery, The First Affiliated Hospital of Jinan University, 510632 Guangzhou, Guangdong, P. R. China. ²State Key Laboratory of Bioactive Molecules and Druggability Assessment/International Cooperative Laboratory of Traditional Chinese Medicine Modernization and Innovative Drug Development of Ministry of Education (MOE) of China/College of Pharmacy, Jinan University, Guangzhou 510632, P. R. China. ³Institute of Precision Cancer Medicine and Pathology, Jinan University Medical College, Guangzhou, Guangdong 510632, P. R. China. ⁴The Affiliated Hospital of Xiangnan University, Chenzhou, Hunan, P.R. China. ⁵Department of Hepatic-biliary-pancreatic Surgery, The Second People's Hospital of Foshan, Foshan, Guangdong 528000, P. R. China. ⁶State Key Laboratory of Bioactive Molecules and Druggability Assessment, Jinan University, Guangzhou 510632, China. ⁷Guangdong Engineering Research Center of Chinese Medicine & Disease Susceptibility, Jinan University, Guangzhou 510632, P. R. China. ⁸These authors contributed equally: Zhan Zhao, Jiashuai He, Shenghui Qiu, Lu Wang, Shuchen Huangfu. ✉e-mail: liutongzheng@jnu.edu.cn; wuyanping@jnu.edu.cn; huajianve@foxmail.com

The treatment of BRAF^{V600E} CRC has always been challenging, with conventional chemotherapy and radiation therapy showing poor efficacy⁶. CRC patients with mutant BRAF hard to respond to BRAF inhibitor therapy due to intrinsic resistance⁷. Currently, targeted therapy for BRAF^{V600E} CRC mainly focuses on key targets of the MAPK pathway, including BRAF, EGFR, and MEK⁸. Although patients with BRAF^{V600E} mCRC have minimal response to BRAF inhibitor monotherapy with vemurafenib⁹, after BRAF blockade, signaling can be reactivated through bypass pathways, leading to loss of efficacy of BRAF inhibition. Based on this finding, a new treatment model involving multitarget blockade of the EGFR + MAPK pathway has been proposed¹⁰. The overall response rate of previously effective dual-target therapy with BRAF inhibitors (BRAFi) and EGFR inhibitors (EGFRi) for BRAF^{V600E} CRC is only 20%¹¹. Combination therapy with BRAF/EGFR/MEK inhibitors provides more promising activity than BRAF/MEK dual therapy¹². However, the BEACON clinical trial¹³ showed that the median survival time of patients with BRAF^{V600E} mCRC treated with BRAF/EGFR/MEK triple combination inhibition was only extended by 4.4 months compared with that with conventional chemotherapy, and there was no significant improvement in clinical benefits compared with BRAF/EGFR dual therapy¹⁴. These data confirm that targeting the BRAF and MAPK pathways has a limited effect. Therefore, identifying regulatory pathways independent of the MAPK pathway in BRAF^{V600E} CRC is the key to breakthrough clinical efficacy.

In this work, we perform a whole-genome clustered regularly interspaced short palindromic repeats (CRISPR)-CRISPR-associated protein 9 (Cas9) screening in human BRAF^{V600E} CRC cells in the context of MAPKi. We find that targeting GPX4 could overcome resistance of BRAFi ± EGFRi in BRAF^{V600E} CRC. Specifically, BRAFi ± EGFRi therapy induces GPX4 upregulated expression, which antagonizes lipid peroxidation and ferroptosis by reactive oxygen species (ROS) caused by BRAFi ± EGFRi intervention. Through integrated proteomics and phosphoproteomics analyses, we reveal that CBX8 phosphorylation promotes GPX4 transcription by BRAFi ± EGFRi. With CBX8 upstream, we discover that polo-like kinase 1 (PLK1) substrate activation facilitates the translocation of PLK1 to the nucleus and activates CBX8 phosphorylation at Ser265, leading to increased GPX4 expression. Targeting PLK1 promotes BRAFi ± EGFRi tumor growth inhibition and triggers ferroptosis in vitro, *in vivo*, organoid, and patient-derived xenograft (PDX) model. Collectively, we demonstrate a PLK1-CBX8-GPX4 signaling axis that relays the ferroptosis mechanism of therapeutic resistance independent of MAPK signaling. Our study suggests a clinically actionable strategy, the addition of PLK1 inhibitors (PLKi) to targeted therapies, to overcome BRAFi ± EGFRi resistance in BRAF^{V600E} CRC.

Results

Enhancement of GPX4 expression is associated with BRAFi ± EGFRi resistance in BRAF^{V600E} CRC

To identify targets involved in response to BRAFi ± EGFRi, we performed genome-wide CRISPR knockout screening in BRAF^{V600E} cell line HT-29¹⁵. The abundance of each single guide RNA (sgRNA) was selectively enriched in BRAFi (LGX818)- or BRAFi + cetuximab-treated HT-29 cells for 14 days using next-generation sequencing (Fig. 1a). Negative screen (loss-of-function screen) of analysis showed sgRNA reads of *GPX4* are depleted in the presence of BRAFi (LGX818) (Fig. 1b, Supplementary Data 1) or BRAFi + cetuximab (Fig. 1c, Supplementary Data 2) compared with DMSO (day 14), suggesting that GPX4 inhibition is synthetically lethal with BRAFi or BRAFi + cetuximab.

To identify pathways responsible for drug resistance to BRAFi or BRAFi + cetuximab in BRAF^{V600E} CRC, we performed proteomics to measure protein changes in HT-29 cells treated with LGX818 ± cetuximab. We further found that GPX4, a key regulatory factor in ferroptosis, had increased expression in HT-29 cells after LGX818 ± cetuximab treatment (Fig. 1d, Supplementary Data 3). KEGG analysis

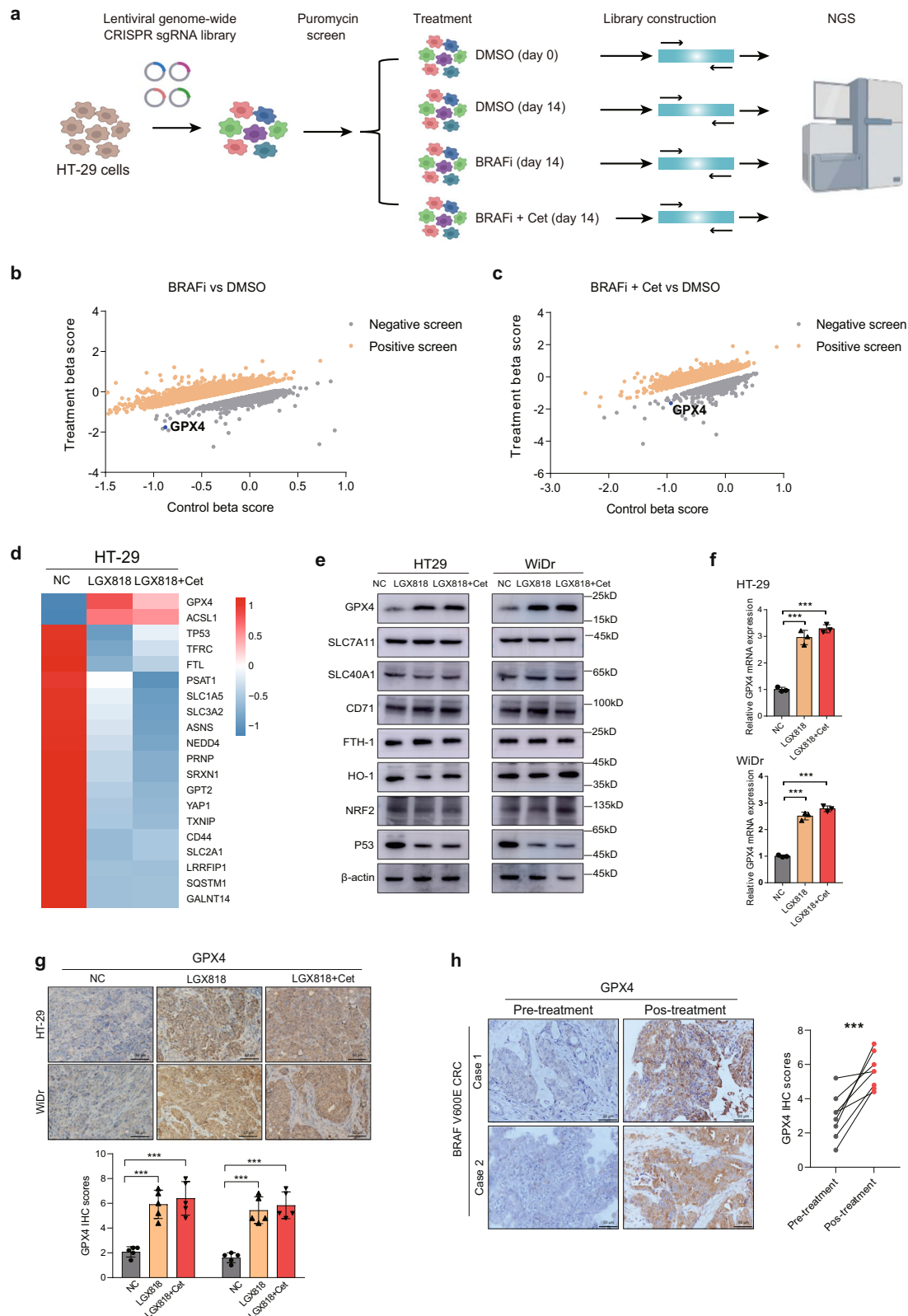
indicated that ferroptosis pathway participates in resistance of BRAF^{V600E} CRC to LGX818 ± cetuximab (Supplementary Fig. 1a–b, Supplementary Data 4–5) associated with inorganic ion and lipid transport and metabolism (Supplementary Fig. 1c–d). We further investigated the effects of LGX818 or LGX818 + cetuximab on ferroptosis-related markers in BRAF^{V600E} CRC cells and found that LGX818 or LGX818 + cetuximab increased GPX4 expression, reduced p53 expression, and did not affect NRF2, SLC7A11, SLC40A1, HO-1, CD71, and FTH1 expressions (Fig. 1e). To confirm that GPX4 upregulated expression in BRAF^{V600E} CRC with LGX818 ± cetuximab treatment, we detected GPX4 expression in BRAF and KRAS wild-type (Wt) cell line Caco2; BRAF (V600E) mutation cell lines HT-29, WiDr, and RKO; and KRAS mutation cell lines DLD1, LoVo, and HCT116 (Supplementary Fig. 2a). Moreover, we further confirmed that LGX818 ± cetuximab increased the GPX4 expression in RKO cell lines (Supplementary Fig. 2b). However, it did not increase the GPX4 expression in Caco2, DLD1, LoVo, and HCT116 cell lines (Supplementary Fig. 2c–d). Moreover, LGX818 ± cetuximab treatment increased GPX4 expression through the mRNA levels in HT-29 and WiDr cell lines (Fig. 1f). An *in vivo* study showed that LGX818 ± cetuximab had a slight inhibition in HT-29 and WiDr xenograft model (Supplementary Fig. 2e), whereas Immunohistochemical (IHC) staining revealed that LGX818 ± cetuximab increased GPX4 expression in tumor tissues (Fig. 1g). These results confirm that BRAFi ± EGFRi intervention enhances GPX4 expression in BRAF^{V600E} CRC.

To evaluate the clinical relevance of GPX4 expression in BRAF^{V600E} CRC, the GPX4 expression of cancer and adjacent normal tissues from a cohort of 44 patients with BRAF^{V600E} CRC was evaluated via IHC. GPX4 expression was higher in cancer tissues than in adjacent normal tissues ($P < 0.001$) (Supplementary Fig. 2f). Additionally, we included another cohort of eight patients (Supplementary Data 6) with BRAF^{V600E} mCRC with BRAFi + EGFRi treatment and compared GPX4 expression before and after BRAFi + EGFRi treatment in the cancer tissue. IHC results showed that GPX4 expression was upregulated after BRAFi + EGFRi treatment ($P < 0.001$) (Fig. 1h). Participants with GPX4-high BRAF^{V600E} CRC had a shorter OS time than those with low GPX4 expression ($P = 0.033$) (Supplementary Fig. 2g, Supplementary Data 7). Collectively, these findings further indicate that BRAFi + EGFRi enhances GPX4 expression and high GPX4 expression correlated with poor prognosis in BRAF^{V600E} CRC.

Synthetic lethal combination targeting GPX4 with BRAF ± EGFR uncovers intrinsic susceptibility of BRAF^{V600E} CRC to ferroptosis

To further investigate the role of GPX4, we generated GPX4 knockdown HT-29 and WiDr cell lines (Supplementary Fig. 3a). Then, we found knockdown GPX4 inhibit HT-29 and WiDr cell proliferation (Supplementary Fig. 3b). Unexpectedly, knockdown of GPX4 in HT-29 and WiDr cell lines had reduced inhibitory concentration 50 (IC₅₀) values in the presence of LGX818 ± cetuximab (Fig. 2a). Knockdown of GPX4 also enhanced the inhibition of clonal formation of LGX818 ± cetuximab at different dose concentrations in HT-29 and WiDr cell lines (Supplementary Fig. 3c). To confirm the potency and synergy of combination targeting GPX4 with BRAF ± EGFR, the IC₅₀ values of GPX4-specific inhibitor RSL3 in HT-29 and WiDr cell lines was also reduced in the presence of BRAFi ± EGFRi (Fig. 2b). When the HT-29 and WiDr cells were treated and combined with BRAF ± EGFR and RLS3, a lethal phenotype was observed when increase the concentration of RLS3 under bright field and PI staining (Supplementary Fig. 4a–b). These results prove the synthetic lethal effect of combination targeting GPX4 with BRAF ± EGFR in BRAF^{V600E} CRC.

We next examined the possible mechanisms underlying the potency of this drug combination strategy. We used the ferroptosis inhibitors Fer-1 and Lip-1, which restored the inhibitory effects of the combination treatment of LGX818 ± cetuximab and RLS3 in HT-29 and WiDr cells (Supplementary Fig. 5). These results further suggest that



the combination treatment triggers ferroptosis in $BRAF^{V600E}$ CRC cells. To confirm this hypothesis, we observed indicators related to ferroptosis after the combination treatment. A significant increase in cellular ROS production after LGX818 ± cetuximab treatment was demonstrated by 2',7'-dichlorodihydrofluorescein diacetate (Fig. 2c). Previous study has suggested mitochondrial ROS production after BRAFi exposure in $BRAF^{V600E}$ melanoma cells¹⁶. The lipid peroxidation level

did not increase after LGX818 ± cetuximab treatment, but a combination of RSL3 rapidly increased the lipid peroxidation level (Fig. 2d). BODIPY-C11 probe and 4-hydroxynonenal (4-HNE) results also confirmed the lipid peroxides in cellular membranes after combining RSL3 with LGX818 ± cetuximab treatment in HT-29 and WiDr cells (Supplementary Fig. 6a–b). These results confirm that enhanced GPX4 expression is the key suppressor for preventing cell membrane lipid

Fig. 1 | Enhanced GPX4 expression is associated with BRAFi ± EGFRi treatment resistance in BRAF^{V600E} CRC. a Flowchart of genome-wide CRISPR screening of BRAFi ± EGFRi-resistant-associated genes. **b, c** CRISPR screening results of BRAFi (LGX818 1 μM) or BRAFi (LGX818 100 nM) + cetuximab (Cet, 100 ng/ml) treatment for 14 days compared with DMSO treatment in HT-29 cells. Gray dots represent BRAFi-resistant or BRAFi + EGFRi-resistant genes. **d** Top 20 differentially expressed ferroptosis-related proteins after indicated treatment in HT-29 cells for 48 h (fold change > 1.5). **e** Western-blot revealed the levels of ferroptosis-related proteins in HT-29 and WiDr treated with LGX818 or LGX818 + Cet. **f** The expression of GPX4

was measured by Rt-qPCR in HT-29 and WiDr cell lines treated with LGX818 or LGX818 + Cet ($n = 3$). **g** Representative IHC images of the GPX4 in HT-29 and WiDr cell-based tumors treated with LGX818 (30 mg kg⁻¹) or LGX818 (10 mg kg⁻¹) + Cet (5 mg kg⁻¹) for 21 days ($n = 5$ mice per group). **h** GPX4 expression in pre- and post-treatment BRAF^{V600E} CRC tissues from anti-BRAF/EGFR-based adjuvant therapy (CRC tissues, $n = 8$). *** $P < 0.001$. Western-blot are representative of three independent experiments (**e**). Data were presented as mean ± SD of three independent experiments (**f**). Data were analyzed by two-sided one-way ANOVA in (**f, g**). Data were analyzed by t test in **h**. Source data are provided as a Source Data file.

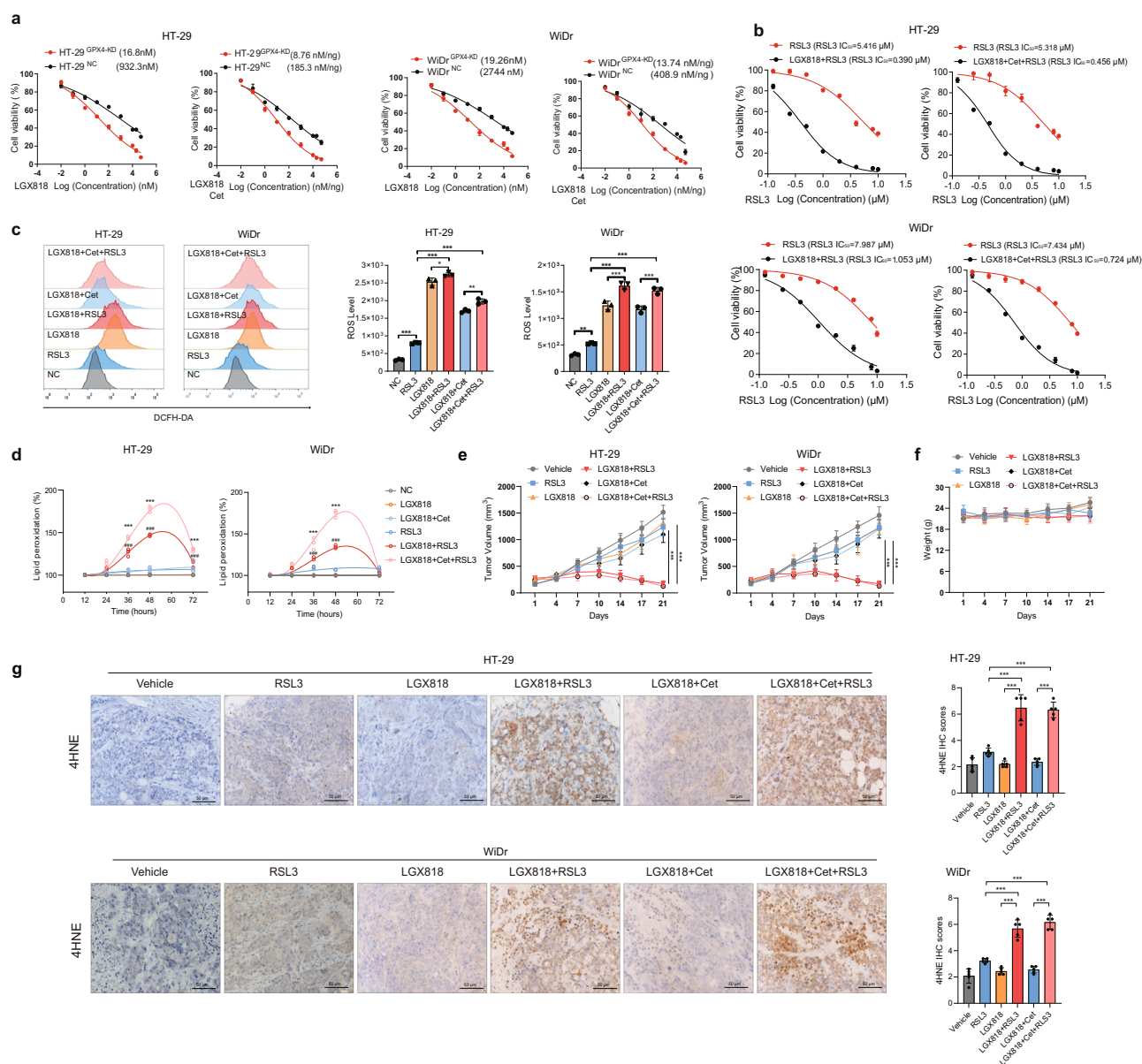


Fig. 2 | GPX4 inhibition induces synthetic lethality combined with BRAFi + EGFRi treatment via ferroptosis in BRAF^{V600E} CRC. a Dose–response curves with IC₅₀ of LGX818 or LGX818 + Cet in HT-29 and WiDr cells with GPX4 knockdown ($n = 3$). **b** Dose–response curves of RSL3 in HT-29 and WiDr cells treated with LGX818 (1 μM) or LGX818 (100 nM) + cetuximab (100 ng/ml). **c** Cellular ROS level after the indicated treatment for 48 h. **d** Effects of lipid oxidation in cell membrane with different treatments for different times were detected by staining with Liperfluor ($n = 3$). *** $P < 0.001$ vs. the LGX818 group; ### $P < 0.001$ vs. the LGX818 + Cet group. **e** Tumor volume of mice bearing HT-29 or WiDr cells treated with

vehicle control, RSL3, LGX818 (30 mg kg⁻¹), LGX818 (30 mg kg⁻¹) + RSL3 (10 mg kg⁻¹), LGX818 (10 mg kg⁻¹) + cetuximab (Cet) (5 mg kg⁻¹), or LGX818 + Cet (5 mg kg⁻¹) + RSL3 (10 mg kg⁻¹) for 21 days ($n = 5$ mice per group). Tumor volumes were calculated every 3 days. **f** Body weight of different groups after indicated treatments ($n = 5$ mice per group). **g** IHC staining and quantification of 4-HNE expression in a subcutaneous tumor model ($n = 5$). * $P < 0.05$, ** $P < 0.01$, *** $P < 0.001$. Data were presented as mean ± SD of three independent experiments (**a, b, c, d**) and five independent experiments (**e, f, g**). Data were analyzed by two-sided one-way ANOVA in (**c–e, g**). Source data are provided as a Source Data file.

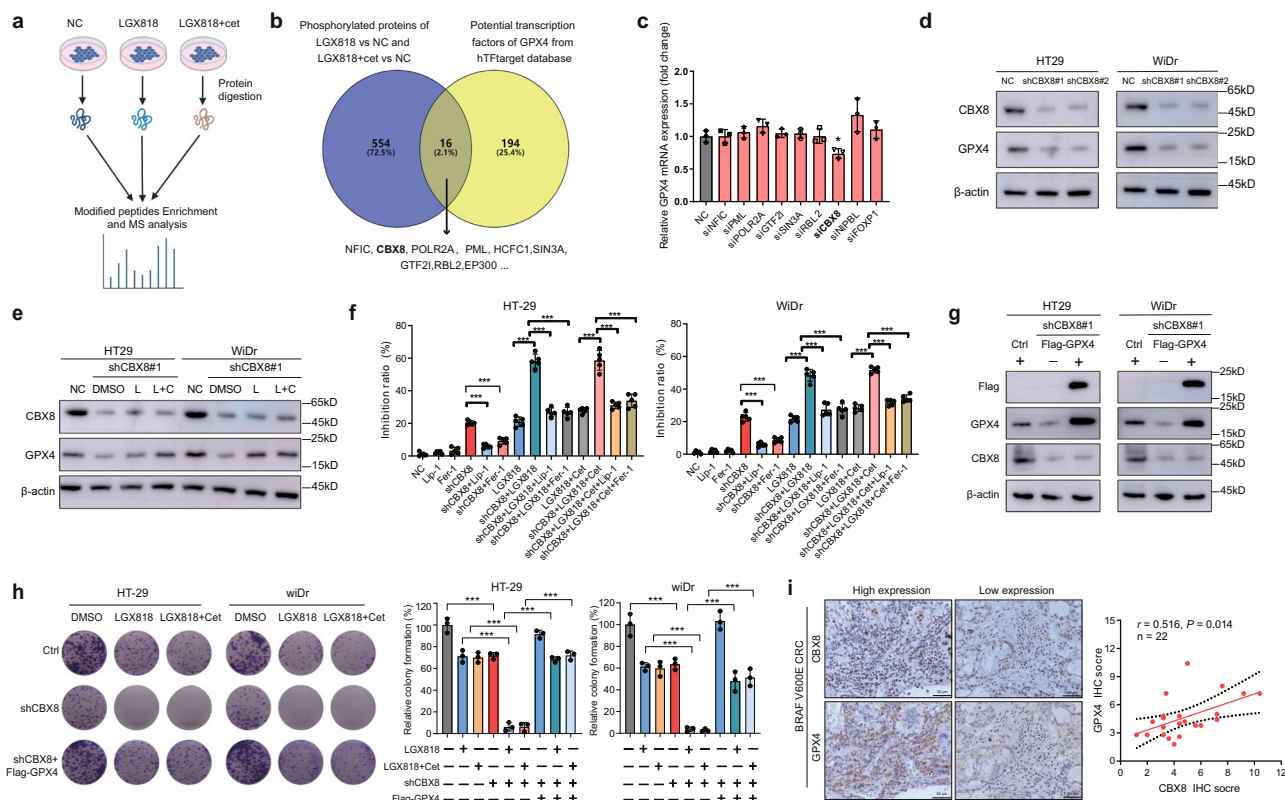


Fig. 3 | CBX8 regulates GPX4 expression under BRAFi + EGFRi treatment in BRAF^{V600E} CRC. **a** Schematic overview of protein phosphorylation modification profiling based on indicated cells. **b** Venn diagram showing the common phosphorylated transcription factors in indicated cells and the hTFtarget database. **c** RT-qPCR revealed the potential transcription factors for regulating GPX4 in HT-29 cells ($n = 3$). **d** GPX4 expressions were detected in CBX8 knockdown cells. **e** Western blot revealed GPX4 expression level in CBX8 knockdown with LGX818 (L) or LGX818 + Cet (L + C) treatment in BRAF^{V600E} CRC cells. **f** Cell viability of CBX8 knockdown

cells after indicated treatment for 48 h ($n = 5$). **g** CBX8 knockdown cells were transfected with Flag-GPX4. **h** Colony formation for CBX8 knockdown and Flag-GPX4 cell lines treated with indicated treatments ($n = 3$). **i** IHC images of the relationship between GPX4 and CBX8 expressions in BRAF^{V600E} CRC tissues ($n = 22$). * $P < 0.05$, ** $P < 0.01$, *** $P < 0.001$. Western blot are representative of three independent experiments. Data were presented as mean \pm SD of three or five independent experiments (**c**, **f**, **h**). Data were analyzed by two-sided one-way ANOVA in (**c**, **f**, **h**). Source data are provided as a Source Data file.

peroxidation induced by BRAFi in BRAF^{V600E} CRC. Next, we found that combining RSL3 with LGX818 \pm cetuximab also increased iron accumulation by Phen Green SK (PGSK) (Supplementary Fig. 6c). The GSH level decreased, whereas the level of oxidative stress marker malondialdehyde (MDA) increased in the combination treatment (Supplementary Fig. 6d–e). Finally, evidently shrunken mitochondria were observed in HT-29 cells of the LGX818 + RSL3 and LGX818 + cetuximab + RSL3 groups (Supplementary Fig. 6f). An in vivo study further showed that combining RSL3 with LGX818 \pm cetuximab treatment had strong inhibitory effects in HT-29 and WiDr xenograft model with tolerable toxicity at the applied doses (Fig. 2e–f). Moreover, IHC results also confirmed the significant 4-HNE enhanced expression after combining RSL3 with LGX818 \pm cetuximab treatment in HT-29 and WiDr tumor tissues (Fig. 2g). Collectively, these results indicate that GPX4 is a dependent target for triggering ferroptosis and synthetic lethality in combination with BRAF \pm EGFR treatment in BRAF^{V600E} CRC.

CBX8 antagonizes BRAFi \pm EGFRi-induced BRAF^{V600E} CRC ferroptosis by the transcriptional regulation of GPX4

GPX4 inhibition may lead to adverse reactions in other organs and tissues, making its wide application in human cancer difficult¹⁷. BRAFi \pm EGFRi treatment inducing GPX4 upregulation in protein and transcription levels is the key for resistance. We further investigated the upstream regulators of GPX4 based on BRAFi \pm EGFRi treatment. 4D-LFQ protein phosphorylation modification omics was used to analyze the differential phosphorylated proteins in LGX818 \pm cetuximab-treated HT-29 cells (Fig. 3a, Supplementary Data 8). Potential

transcription factors of GPX4 were searched in the hTFtarget database, taking the intersection of the two datasets for the potential phosphorylated transcription factor of GPX4 for further verification (Fig. 3b, Supplementary Data 9). To further identify the transcription factors of GPX4, we used siRNAs targeting nine potential phosphorylated transcription factors of GPX4 to screen for potential targets regulating GPX4 expression. Each of these siRNAs was individually transfected into HT-29 cells, followed by the analysis of knockdown expression (Supplementary Fig. 7). Among the nine siRNAs, only the knockdown of CBX8 reduced GPX4 mRNA expression (Fig. 3c) with or without LGX818 \pm cetuximab treatment (Supplementary Fig. 8a–b). CBX8 is an essential component of the polycomb repressive complex, which directly regulates the expression of numerous target genes¹⁸. CBX8 knockdown also reduced the GPX4 protein levels in HT-29 and WiDr cells (Fig. 3d). Moreover, CBX8 mediated GPX4 increase in protein level under the LGX818 \pm cetuximab treatment in HT-29 cells (Fig. 3e). These results indicate that CBX8 is a key activated transcription factor for GPX4 expression in BRAF^{V600E} CRC.

Subsequently, we hypothesized that CBX8 was involved in BRAFi \pm EGFRi-induced BRAF^{V600E} CRC cell ferroptosis. CBX8 knockdown increased the inhibition rate of LGX818 \pm cetuximab in HT-29 and WiDr cells, whereas Fer-1 or Lip-1 reduced the inhibitory effects of CBX8 knockdown and the combination treatment of LGX818 \pm cetuximab + CBX8 knockdown HT-29 and WiDr cells (Fig. 3f). Moreover, CBX8 knockdown further increased cellular ROS production induced by LGX818 \pm cetuximab in HT-29 and WiDr cells (Supplementary Fig. 9a) and triggered the increase in lipid peroxidation levels

(Supplementary Fig. 9b). Next, GSH level decreased, whereas MDA level increased in the combination of knockdown CBX8 and LGX818 ± cetuximab treatment (Supplementary Fig. 9c–d). Moreover, CBX8 knockdown also increased iron accumulation in HT-29 and WiDr cells in combined LGX818 ± cetuximab treatment (Supplementary Fig. 9e). To further confirm that targeting CBX8 promoted LGX818 ± cetuximab-induced ferroptosis in BRAF^{V600E} CRC, colony formation assay showed that GPX4 overexpression in CBX8 knockdown HT-29 and WiDr cells restored drug resistance to LGX818 ± cetuximab (Fig. 3g, h). Our CRISPR screening result also showed that CBX8 was a negative regulatory target in LGX818 ± cetuximab treatment (Supplementary Fig. 9f). Furthermore, IHC analysis of 22 BRAF^{V600E} CRC tissues

with serial section showed that CBX8 positively correlated with GPX4 protein expression (Fig. 3i). Thus, these results confirm that CBX8 promotes LGX818 ± cetuximab-induced ferroptosis in BRAF^{V600E} CRC-dependent GPX4.

To further reveal the mechanism by which CBX8 regulates GPX4 expression, we identified four CBX8 potential binding sites in the BS1 (−1421 to −1414, GTGACTCA), BS2 (−1160 to −1154, ATGACTC), and BS3 (−790 to −784, TGAGTCA) regions of the GPX4 promoter (Fig. 4a). Subsequently, we constructed GPX4 promoter-driven luciferase reporter plasmids containing the full-length GPX4 promoter or its different deletion fragments. As shown in Fig. 4b, 293 T cells transfected with the GPX4 promoter fragment (−2068/+1) showed a clear

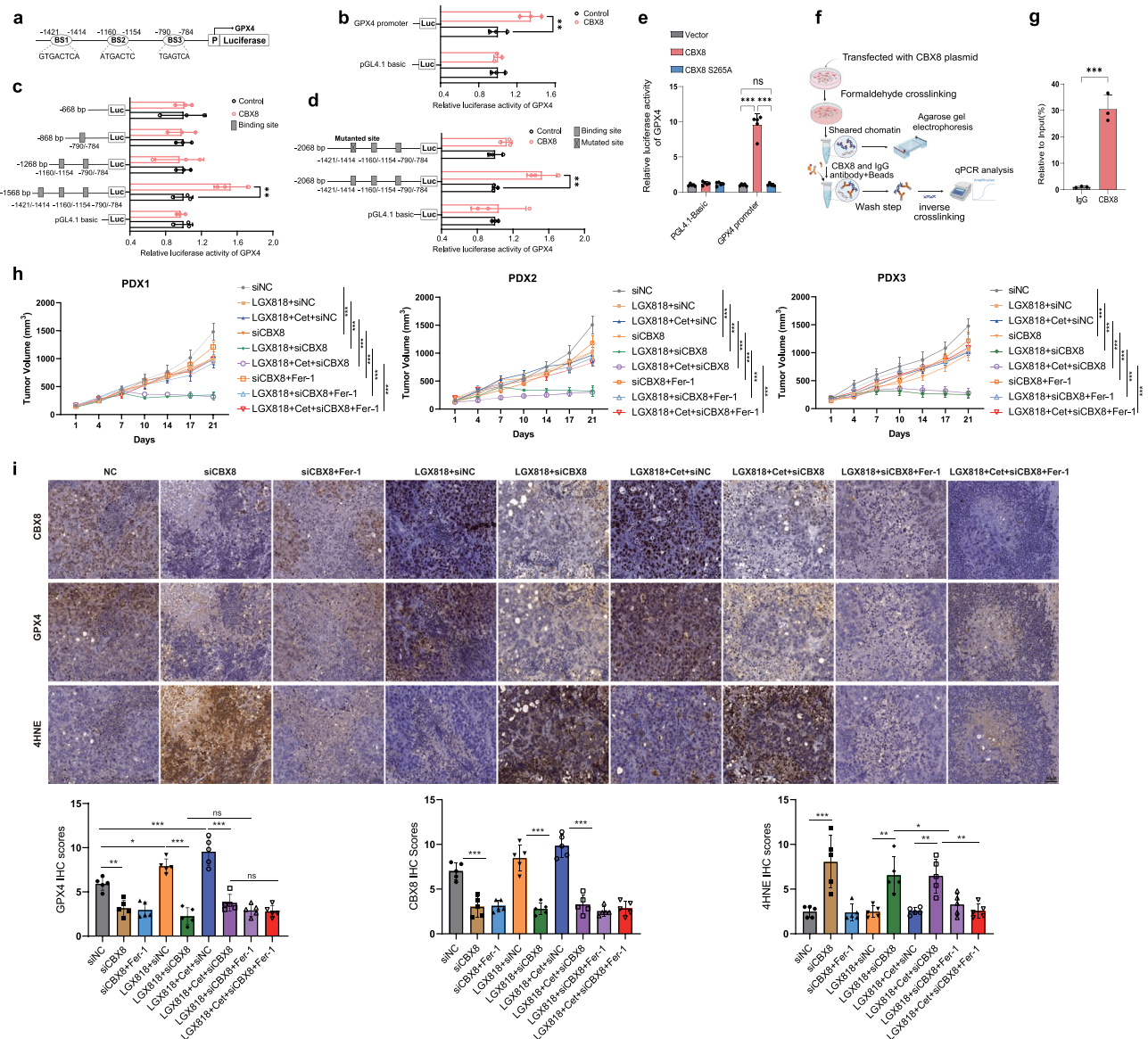


Fig. 4 | CBX8 transcriptional upregulates GPX4 in BRAF^{V600E} CRC. **a** A 2068 bp fragment of promoter region of GPX4 was cloned into the pGL4.1 vector, including three potential binding sites (BS), BS1 (−1421 to −1414, GTGACTCA), BS2 (−1160 to −1154, ATGACTC), and BS3 (−790 to −784, TGAGTCA) from the GPX4 promoter. **b** Dual-luciferase reporter assay was detected GPX4 promoter activity after CBX8 overexpressed 293 T cells ($n = 3$). **c** Promoter region of GPX4 was cloned into the pGL4.1 vector, including a 668 bp fragment without potential BS, an 868 bp fragment with BS3, a 1268 bp fragment with BS2 and BS3, and a 1568 bp fragment with BS1, BS2, and BS3 from the GPX4 promoter ($n = 3$). **d** Dual-luciferase reporter assay was detected GPX4 promoter activity after BS1 mutation ($n = 3$). **e** Dual-luciferase

reporter assay was detected GPX4 promoter activity after CBX8 WT or S265A overexpressed in 293 T cells ($n = 5$). **f–g** ChIP-qPCR was performed with CBX8-specific antibody ($n = 3$). **h** Tumor growth inhibition in three BRAF^{V600E} CRC PDX models following with indicated treatments ($n = 5$ mice per group), LGX818 (30 mg kg^{−1}), LGX818 (10 mg kg^{−1}) + Cet (5 mg kg^{−1}), Fer-1 (10 mg kg^{−1}). **i** IHC staining and quantification of CBX8, GPX4 and 4-HNE expression in a subcutaneous tumor model ($n = 5$). Data represent mean ± SD, * $P < 0.05$, ** $P < 0.01$, *** $P < 0.001$. Data were presented as mean ± SD of three or five independent experiments (**b–e**, **h**, **i**) and by t test in **g**. Source data are provided as a Source Data file.

induction of luciferase activity with increasing amounts of CBX8. Further verification experiments found that the -1421 to -1414 region was crucial to the transcription activation of GPX4 by CBX8 (Fig. 4c) and that mutation of -1421 to -1414 region of GPX4 promoter showed no significant increased luciferase activity by CBX8 (Fig. 4d). Base on the LGX818 ± cetuximab treatment and CBX8 overexpression, WiDr cell with full-length GPX4 promoter reporter has higher luciferase activity compared with LGX818 ± cetuximab or CBX8 overexpression alone (Supplementary Fig. 10a). Further verification experiments found that the -1421 to -1414 region was crucial to the transcription activation of GPX4 by CBX8 base on the LGX818 ± cetuximab treatment (Supplementary Fig. 10b). As Ser265(S265) was a major phosphorylation site on CBX8 under LGX818 ± cetuximab treatment (Supplementary Data 8), S265A mutant of CBX8 can not enhance the luciferase activity of GPX4 promoter compared with CBX8-WT (Fig. 4e). We further performed ChIP-Quantitative Polymerase Chain Reaction (ChIP-qPCR) assays, and confirmed the binding of CBX8 at the GPX4 gene promoter region (Fig. 4f, g). Therefore, these results further confirm LGX818 ± cetuximab activates CBX8, then transcriptional binding on -1421 to -1414 region of GPX4 promoter to increase GPX4 expression.

At last, we used BRAF^{V600E} CRC PDX models to assess for targeting CBX8 combined with BRAFi ± EGFRi whether via ferroptosis. Knocking-down CBX8 combined with LGX818 ± cetuximab sensitizes tumor inhibitory effects, but Fer-1 restored the effects with combination treatment (Fig. 4h). And the IHC results showed targeting CBX8 combined with LGX818 ± cetuximab reduce GPX4 and enhance 4HNE expression, and treated with Fer-1 reducing the 4HNE expression (Fig. 4i). Taken together, these results demonstrate that CBX8 antagonizes BRAFi ± EGFRi-induced BRAF^{V600E} CRC ferroptosis by transcriptionally upregulating GPX4 expression.

Activated PLK1 translocates into the nucleus and phosphorylates Ser265 of CBX8

As we observed CBX8 phosphorylation and transcriptional regulation of GPX4 expression, we further studied the upstream mechanism of CBX8 phosphorylation. To identify the kinase activated for CBX8 phosphorylation in BRAF^{V600E} CRC cells, we performed an immunoprecipitation (IP) assay using cell lysates from Flag-CBX8 transfected HT-29 cells with anti-Flag affinity beads. After extensive washing, IP of the protein complexes was visualized via silver staining using sodium dodecyl sulfate-polyacrylamide gel electrophoresis and subjected to mass spectrometry analysis (Fig. 5a). Several proteins, including PLK1, were associated with CBX8 (Fig. 5a). The interaction between PLK1 and CBX8 was also confirmed via endogenous co-IP and in vitro pull-down assays (Fig. 5b–c). We hypothesized that PLK1 could phosphorylate CBX8. It was observed that interaction of PLK1 and CBX8 was increased following treatment with LGX818 alone or in combination with Cetuximab (Fig. 5d). We found that LGX818 ± cetuximab treatment increased the total serine phosphorylation of CBX8 and that knocking down PLK1 expression could antagonize the total serine phosphorylation of CBX8 mediated by LGX818 ± cetuximab (Fig. 5e). LGX818 or LGX818 + Cetuximab treatment do not increase CBX8 expression level, but increase CBX8 phosphorylation level in S265 (Fig. 5f). Moreover, knocking down PLK1 expression could enhance the anti-tumor effect of LGX818 ± cetuximab on HT29 cells (Supplementary Fig. 11). Furthermore, to test whether PLK1 regulates GPX4 expression, we knocked down the expression of CBX8 or combined it with onvansertib (Onva), a PLK1 inhibitor that can inhibit GPX4 expression at the protein and mRNA levels (Fig. 5g, h).

We found that Ser265(S265) was a major phosphorylation site on CBX8 under LGX818 ± cetuximab treatment (Supplementary Data 8, Supplementary Fig. 12). To test whether S265 of CBX8 is a PLK1 phosphorylation site, Flag-fused WT CBX8 and S265A mutant vectors were transfected into CBX8 knockdown HT-29 cells, and a phospho-

Ser265-specific antibody was generated to further study the phosphorylation of Ser265 in cells. As shown in Fig. 5i, WT CBX8 was phosphorylated in cells. However, S265A mutation completely abrogated the phosphorylation of CBX8 at this site, indicating the specificity of this antibody. Next, we tested PLK1-mediated phosphorylation of CBX8 in HT-29 cells. PLK1 inhibition reduced the phosphorylation of CBX8 at Ser265 (Fig. 5j). Furthermore, *PLK1* knockdown in HT-29 cells decreased the phosphorylation of CBX8 at Ser265 (Fig. 5k). Under the intervention of LGX818 + cetuximab, the phosphorylation of CBX8 at 265S was reduced by Onva intervention in HT-29 cells (Fig. 5l). To assess whether PLK1 actions are mediated through the PLK1–CBX8–GPX4 axis, we expressed WT CBX8, S265A, or S265D mutant in HT-29 cells depleted of endogenous CBX8 and then treated these cells with either vehicle or Onva. We found that Onva induced a decrease in GPX4 protein levels only in WT CBX8-reconstituted cells but not in cells reconstituted with S265A or S265D mutants (Fig. 5m). Further, PLK1i can inhibit phosphorylation of CBX8 at Ser265 and antagonize LGX818 ± cetuximab mediated GPX4 up-regulated, S265D CBX8 can rescue PLK1i effect on GPX4 under LGX818 ± cetuximab treatment (Supplementary Fig. 13a). Meanwhile, colony formation assay further showed PLK1 inhibitors mediated synthetic lethality through phosphorylation of CBX8 at 265S (Supplementary Fig. 13b). And the lipid peroxidation level in the S265A CBX8 was earlier than the S265D CBX8 in HT-29 shCBX8 cells (Supplementary Fig. 13c). These results proving that synergy of PLK1i and BRAFi ± EGFRi is mediated through phosphorylation of CBX8 at 265S. To further assess the interaction between PLK1 and CBX8, immunofluorescence (IF) was performed to the location of PLK1 and CBX8. LGX818 or LGX818 + cetuximab treatment promoted PLK1 translocation into the nucleus and CBX8 binding, whereas the combination with Onva inhibited LGX818 or LGX818 + cetuximab-mediated PLK1 translocation into the nucleus (Supplementary Fig. 14a). Then, we also found the active PLK1 could phosphorylate GST-CBX8 WT, but not the S265A mutant in vitro (Fig. 5n). To further confirm whether LGX818 ± cetuximab regulates GPX4 expression via the PLK1–CBX8 axis, we expressed WT CBX8 or S265A mutants in HT-29 cells and then treated these cells with LGX818 ± cetuximab or combined with Onva. We found that Onva reduced GPX4 protein level in WT CBX8 and S265A mutant HT-29 cells under LGX818 ± cetuximab treatment (Fig. 5o). Finally, IHC analysis of 22 BRAF^{V600E} CRC tissues with serial section showed that PLK1 was positively correlated with GPX4 protein expression (Supplementary Fig. 14b). Thus, these findings provide evidence that LGX818 ± cetuximab activates PLK1 translocation into the nucleus and phosphorylates Ser265 of CBX8, which in turn regulates GPX4 expression level.

Targeting PLK1 triggers ferroptosis combined with BRAFi ± EGFRi in BRAF^{V600E} CRC

As the PLK1–CBX8 axis is critical for regulating GPX4 expression in BRAF^{V600E} CRC, we next examined whether targeting PLK1 triggers ferroptosis in BRAF^{V600E} CRC under BRAFi ± EGFRi treatment. And we found that knocking down PLK1 sensitizes tumor inhibition of LGX818 ± cetuximab in BRAF^{V600E} CRC PDX models, and Fer-1 can alleviate the tumor inhibition effects (Fig. 6a). PLK1 knock-down increased the inhibition rate of LGX818 ± cetuximab in HT-29 and WiDr cells, whereas Fer-1 or Lip-1 alleviated the inhibitory effects of the combination treatment (Supplementary Fig. 15a–b). Our CRISPR screening result also showed that PLK1 was a negative regulatory target in LGX818 ± cetuximab treatment (Supplementary Fig. 15c). We used the BRAF^{V600E} CRC cell line to test the effect of ferroptosis. *PLK1* knock-down induced slightly increased ROS in HT-29 and WiDr cells but did not lead to a significant enhancement of lipid peroxidation levels, whereas the combination of *PLK1* knock-down with LGX818 ± cetuximab enhanced ROS and lipid peroxidation levels compared with LGX818 or LGX818 + cetuximab in HT-29 and WiDr cells (Supplementary Fig. 15d–e). We also found that GSH level decreased and MDA level

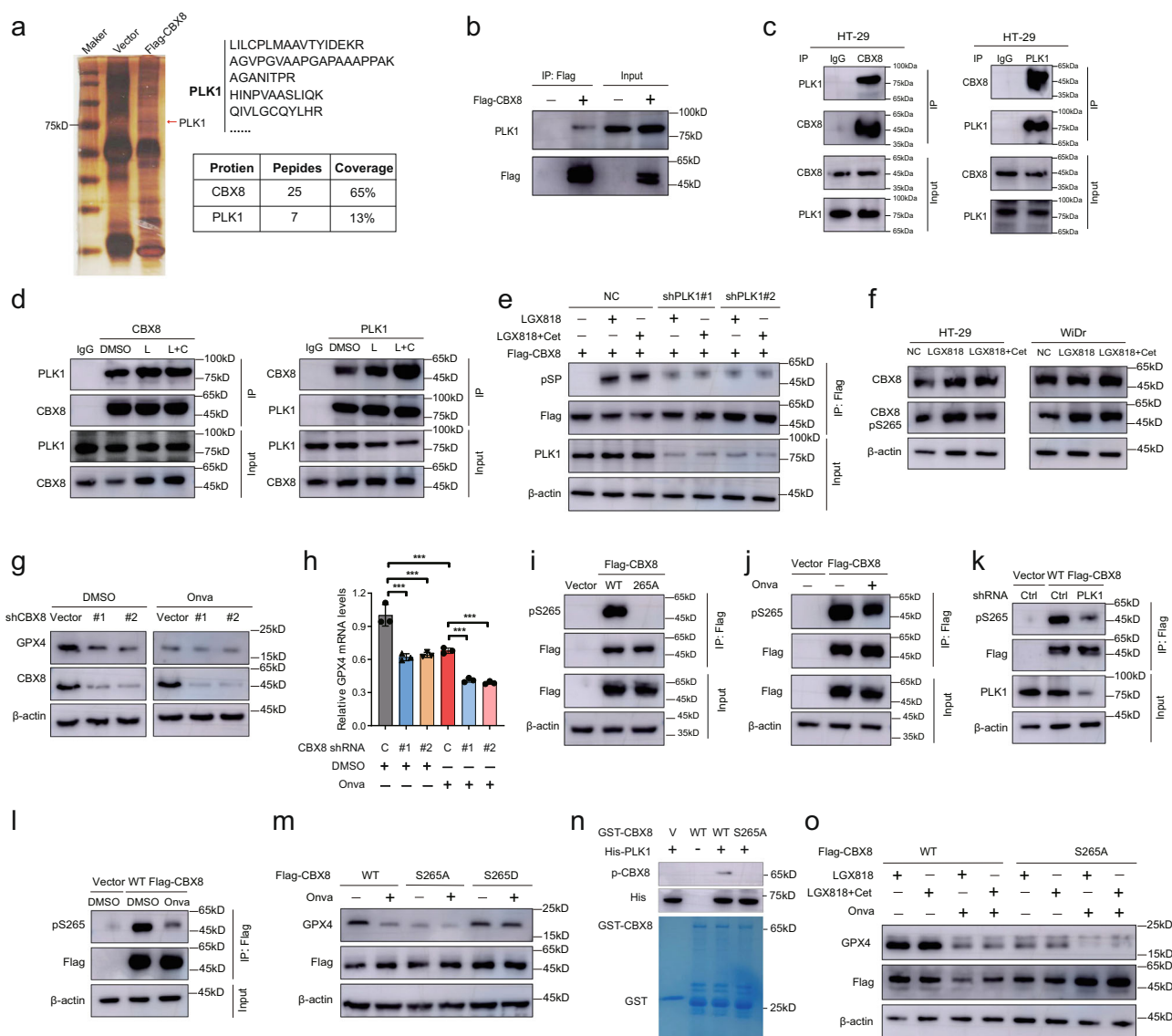


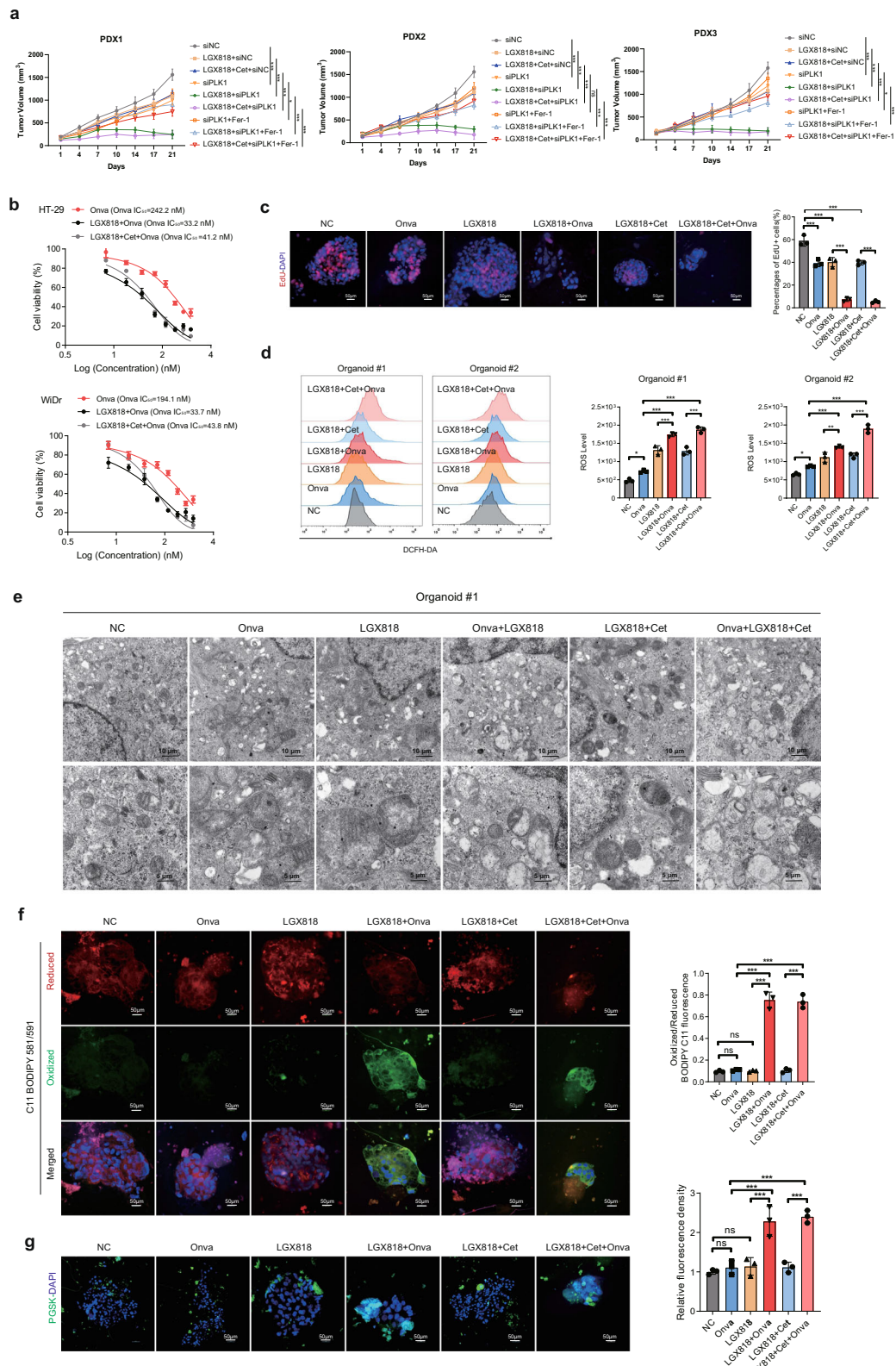
Fig. 5 | PLK1 activation and phosphorylates Ser265 of CBX8, mediating GPX4 upregulation in BRAF^{V600E} CRC. a Silver staining and mass spectrometry analysis of CBX8 immunoprecipitation (IP) complex in HT-29 cell. **b** HT-29 cells were transfected with CBX8. IP and western-blot assays were performed with indicated antibodies. **c** Co-IP showed interaction between PLK1 and CBX8 in HT-29 cells. **d** Co-IP assay for PLK1 and CBX8 interaction in the presence of BRAFi±EGFRi treatment. **e** The total serine phosphorylation of CBX8 was detected in PLK1 knockdown and CBX8 overexpressed HT-29 cells with indicated treatments. **f** Western-blot for CBX8 expression and phosphorylation levels at Ser265 under LGX818 ± cet treatment. **g** CBX8-knockdown HT-29 cells were treated with onvansertib (Onva) (100 nM) for 48 h. Western-blot was performed with the indicated antibodies. **h** RT-qPCR of GPX4 expression in CBX8-knockdown HT-29 cells with indicated treatments ($n = 3$). **i** Flag-CBX8 WT or Flag-CBX8 S265A was transfected in cells. **j** CBX8

overexpressed HT-29 cells were treated with Onva. **k** CBX8 overexpressed HT-29 cells were transfected with PLK1 shRNA, IP and western-blot assays were performed with indicated antibodies. **l** Under the intervention of LGX818 + Cet, HT-29 cells were transfected with indicated plasmids and were treated with Onva, and the indicated antibody was examined. **m** Western-blot was performed with the indicated antibodies in CBX8 knockdown HT-29 cells treated with Onva. **n** Purified recombinant His-PLK1 were incubated with GST or GST-CBX8 WT or GST-CBX8 S265A and the direct interaction between PLK1 and CBX8 was examined. **o** Western-blot was performed with the indicated antibodies in cells. Data represent mean ± SD, * $P < 0.05$, ** $P < 0.01$, *** $P < 0.001$. Western-blot are representative of three independent experiments. Data were presented as mean ± SD of three independent experiments (**h**). Data were analyzed by two-sided one-way ANOVA in **h**. Source data are provided as a Source Data file.

increased in the combination of PLK1 knock-down and LGX818 ± cetuximab treatment in HT-29 and WiDr cells (Supplementary Fig. 15f-g). PGSK results also showed increased cellular iron levels after PLK1 knock-down and LGX818 ± cetuximab treatment in HT-29 and WiDr cells (Supplementary Fig. 15h). Transmission electron microscopy (TEM) showed a shrunken mitochondria characteristics in the HT-29 cells after Onva + LGX818 ± cetuximab treatment (Supplementary Fig. 15i).

To further confirm the ferroptosis of targeting PLK1 in BRAF^{V600E} CRC combined with BRAFi ± EGFRi, we test the IC₅₀ of PLK1 inhibitor in combination treatment. LGX818 ± cetuximab treatment reduced IC₅₀

Onva values for the inhibition of HT-29 and WiDr cells (Fig. 6b). Synergetic inhibition combined Onva with LGX818 ± cetuximab, which can be rescue by Fer-1 or Lip-1 (Supplementary Fig. 16a). Overexpression GPX4 reduce the inhibition effect of combination of BRAF ± EGFRi and PLK1 inhibition in HT-29 and WiDr cells, these results demonstrate that targeting PLK1 enhance BRAFi ± EGFRi inhibition via GPX4 (Supplementary Fig. 16b). Furthermore, we used 50 nM Onva for further pharmacological studies in BRAF^{V600E} CRC organoid models. Next, Onva + LGX818 ± cetuximab intervention promoted BRAF^{V600E} CRC organoid inhibition in the bright field and EdU assay



(Supplementary Fig. 16c, Fig. 6c). Moreover, Onva + LGX818 ± cetuximab enhanced ROS production compared with LGX818 or LGX818 + cetuximab in BRAF^{V600E} CRC organoids after Onva + LGX818 or Onva + LGX818 + cetuximab treatment also promoted reduced mitochondrial characteristics under TEM (Fig. 6e). Lipid peroxides in cellular membranes and cellular iron levels in organoids also increased after Onva + LGX818 or Onva + LGX818 +

cetuximab treatment (Fig. 6f-g). These results demonstrate that targeting PLK1 promotes LGX818 ± cetuximab, inhibiting BRAF^{V600E} CRC via ferroptosis.

PLK1 is a mitotic kinase that actively regulates G2/M transition, mitosis, mitotic exit, and cytokinesis¹⁹. We examined the cell cycle after Onva + LGX818 or Onva + LGX818 + cetuximab treatment in HT-29 and WiDr cells. PLK1 inhibition enhanced the G2/M stage proportion,

Fig. 6 | Targeting PLK1 triggers ferroptosis combined with BRAFi ± EGFRi in BRAF^{V600E} CRC organoids. **a** Tumor growth inhibition in three BRAF^{V600E} CRC PDX models following with indicated treatments ($n = 5$ mice per group), LGX818 (30 mg kg⁻¹), LGX818 (10 mg kg⁻¹) + Cet (5 mg kg⁻¹), Fer-1 (10 mg kg⁻¹). **b** Dose-response curves with inhibitory concentration of Onva or in combination with LGX818 (1 μM) or LGX818 (100 nM) + cetuximab (100 ng/ml) in HT-29 and WiDr cells. Cell viability was determined using the Cell Counting Kit-8 assay ($n = 3$). **c** Edu assays of BRAF^{V600E} CRC organoids treated with indicated regimen for 4 days. **d** ROS level of organoid was analyzed by flow cytometer ($n = 3$). **e** TEM revealed a

distinctive morphological feature of ferroptosis in BRAF^{V600E} CRC organoids subject to PLK1i combination treatment. **f** Fluorescence images of C11-BODIP in BRAF^{V600E} CRC organoids with indicated treatment ($n = 3$). Reduced: red, oxidized: green. **g** PGSK (green) assay after the indicated treatment BRAF^{V600E} CRC organoids ($n = 3$). Data represent mean ± SD, ns: no significant difference, * $P < 0.05$, ** $P < 0.01$, *** $P < 0.001$. Data were presented as mean ± SD of three or five independent experiments (**b–d, f, g**). Data were analyzed by two-sided one-way ANOVA in (**a, c, d, f, g**). Source data are provided as a Source Data file.

whereas LGX818 ± cetuximab promoted G0/G1 and S stage proportion. The combination of Onva + LGX818 or Onva + LGX818 + cetuximab also enhanced the G2/M stage proportion compared with LGX818 ± cetuximab or enhanced G0/G1 and S stage proportion compared with Onva only, and ferrostatin-1 do not impact the cell cycle in addition to shPLK1 or LGX818 ± cetuximab or the combination treatment (Supplementary Fig. 15j). These results reveal that the combination effect of PLK1 + BRAFi ± EGFRi also has synergetic effect on cell cycle arrest.

Coordinated targeting of PLK1 with BRAF + EGFR improves efficacy in BRAF^{V600E} CRC cells and patient-derived xenograft models

PLK1 is a promising drug target, given its robust association with CRC tumor progression in patients²⁰, although no prior clinical trials have focused on BRAF^{V600E} CRC. Our study found that PLK1i represented a potential combination therapeutic strategy of BRAFi ± EGFRi in BRAF^{V600E} CRC. Several inhibitors (adenosine triphosphate competitors) have been synthesized and have shown activity in both in vitro and in vivo preclinical models²¹. Onva and Vola have been approved by the Food and Drug Administration (FDA) as a breakthrough therapy and orphan drug status, respectively²². Thus, the next step was to test whether the addition of PLK1i could improve BRAFi + EGFRi clinical benchmark regimens: encorafenib + cetuximab¹², vemurafenib + cetuximab²³, and vemurafenib + erlotinib²⁴. The Onva combined with encorafenib (LGX818) ± cetuximab systematically improved the efficacy of other BRAF^{V600E} CRC cell lines, including VAC0432, KM20, RKO-1, and LIM2405 (Fig. 7a). Addition of Onva also improved the efficacy of –and synergized with–vemurafenib ± cetuximab and vemurafenib + erlotinib (Fig. 7b–c). Another PLK inhibitor Vola also showed significant synthetic lethal effect combined with LGX818 ± cetuximab in BRAF^{V600E} CRC cell lines (Fig. 7d). These results demonstrate that the PLK1-based triple therapy is effective in multiple BRAF^{V600E} CRC cell lines.

Finally, we used the in vivo and BRAF^{V600E} CRC PDX models to assess for further therapeutic effects and toxicological studies. An in vivo study showed that the combination of Onva with LGX818 ± cetuximab treatment also had strong inhibitory effects in HT-29 and WiDr xenograft model (Fig. 7e). Toxicology studies result showed that mouse weight, a surrogate for drug toxicity, remained stable over the course of therapy for Onva with LGX818 ± cetuximab combination treatment (Fig. 7f). Compared with the control or LGX818 ± cetuximab group, the Onva + LGX818 and Onva + LGX818 + cetuximab groups had no pathological changes in the lung, heart, liver, spleen, and kidney via microscopic examination (Supplementary Fig. 17). Most importantly, the critical finding from the efficacy studies was that addition of Onva to the LGX818 ± cetuximab drug regimens resulted in consistently superior tumor growth inhibition in all three BRAF^{V600E} CRC PDX models (Fig. 7g). The serial section of IHC of PDX tumor tissues showed that the Onva + LGX818 and Onva + LGX818 + cetuximab groups reduced GPX4 expression and enhanced 4-HNE expression, and Fer-1 can alleviate these effects (Fig. 7h), further confirming that the addition of Onva to the LGX818 ± cetuximab treatment resulted in tumor growth inhibition via ferroptosis in BRAF^{V600E} CRC. These results indicate that PLK1 inhibition represents a low-toxicity drug-repurposing strategy to overcome therapeutic resistance in BRAF^{V600E} CRC and that

supplementing standard-of-care BRAFi + EGFRi with PLK1i durably improves tumor growth inhibition.

Discussion

In our study, we demonstrated that targeting BRAF ± EGFR enhanced GPX4 expression and antagonized lipid peroxidation induced by BRAFi ± EGFRi, and combining with targeting GPX4 triggered ferroptosis and overcame resistance of BRAF + EGFR doublet regimen in BRAF^{V600E} CRC. Activation of PLK1 in response to BRAF ± EGFR therapy is another regulatory pathway independent of the MAPK pathway, and we found that PLK1 activation phosphorylated Ser265 of CBX8, which regulated transcriptional reprogramming and mediated GPX4 upregulated expression. The addition of PLK1, such as Onva, to inhibitor combinations tested in clinical trials consistently resulted in superior and durable tumor growth suppression in BRAF^{V600E} CRC PDX models. Our study identified unanticipated synthetic lethal dependencies of actionable targets, yielding strategies for overcoming therapeutic resistance in BRAF^{V600E} CRC via ferroptosis (Fig. 8).

The lipid peroxidase pathway is a characteristic feature of several therapy-resistant cancers²⁵. A previous study indicated that the sensitivity of individual cell lines to ferroptosis might be influenced by the overall activity of the RAS-RAF-MEK pathway²⁶. However, several unknown factors affect the sensitivity to ferroptosis. In our study, we demonstrated that BRAFi ± EGFRi induced GPX4 high expression in BRAF^{V600E} CRC. Higher GPX4 expression was also correlated with poor prognosis in patients with BRAF^{V600E} CRC. We found the BRAF^{V600E} CRC cells resistant to BRAFi ± EGFRi increased cellular ROS production, but the high cellular ROS production did not induce cell membrane lipid peroxidation in this state. This result also strongly indicates that enhanced GPX4 expression prevents cell membrane lipid peroxidation because GPX4 is the only GSH peroxidase used for intracellular lipid peroxide reduction²⁷. In our CRISPR screening results, GPX4 was identified as one of the most critical negative regulatory factors in the top range. Proteomics also showed that the ferroptosis pathway was involved in the resistance of BRAFi to EGFRi. Another ferroptosis-related target, SLC7A11, had a negative effect in a single drug of BRAFi, but not in BRAFi ± EGFRi, based on our CRISPR screening results. Other ferroptosis-related regulators, such as NRF2, p53, SLC40A1, HO-1, CD71, and FTH1, showed no significant tendency to inhibit ferroptosis. Therefore, we confirm the enhanced GPX4 is the most critical factor for resistance of BRAFi ± EGFRi in BRAF^{V600E} CRC.

Our finding reveals an epigenetic regulation mechanism of GPX4. We identified CBX8 phosphorylation and promoted the transcriptional upregulation of GPX4 in BRAF^{V600E} CRC when treated with BRAFi ± EGFRi. CBX8 is a cancer stemness-related gene associated with poor prognosis in patients with CRC²⁸. We confirmed the CBX8 binding site (–1421 to –1414 region) on the promoter of GPX4 and further found that targeting CBX8 could trigger ferroptosis by regulating GPX4 in BRAF^{V600E} CRC. Moreover, we found that phosphorylation of CBX8 Ser265 was critical for the transcriptional upregulation of GPX4 in BRAF^{V600E} CRC. A previous report suggested that regulatory phosphorylation of CBX8 contributed to its transcriptional activity²⁹. GPX4 and CBX8 lack FDA-approved targeting inhibitors, which limits further clinical application of BRAF^{V600E} CRC. We demonstrated that PLK1 was upstream of CBX8 and that CBX8 was under the regulatory control of

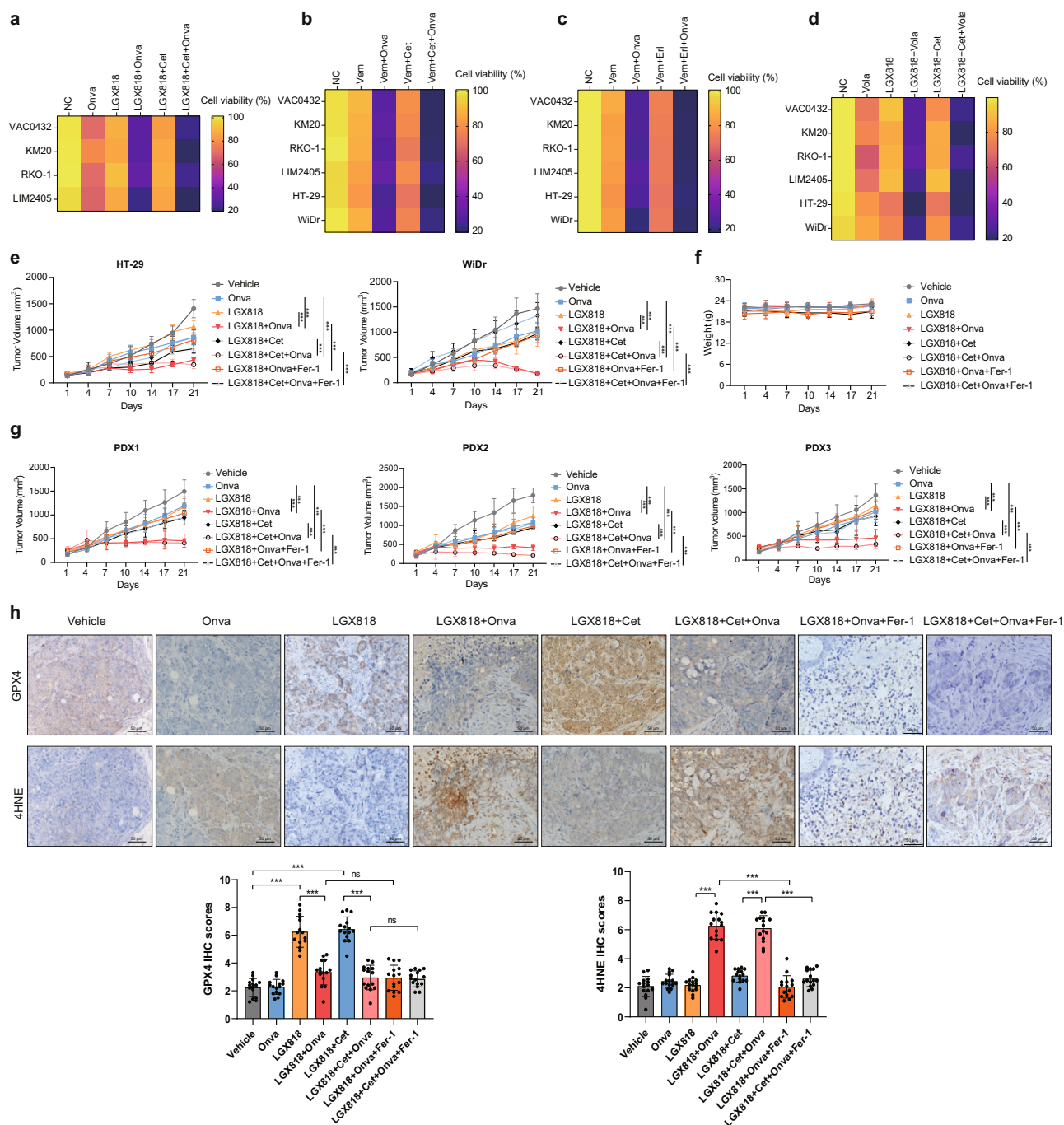


Fig. 7 | Coordinated targeting of PLK1 + BRAF + EGFR improves efficacy in BRAF^{V600E} CRC cell lines and patient-derived xenograft (PDX) models.

a–d Heatmap indicating the effect of the indicated regimen for 48 h on the cell viability of BRAF^{V600E} CRC cell lines. **e** Mice bearing HT-29, WiDr xenografted tumors were treated with Onva (10 mg kg⁻¹), LGX818 (30 mg kg⁻¹), LGX818 (10 mg kg⁻¹) + Cet (5 mg kg⁻¹), Fer-1 (10 mg kg⁻¹) for 21 days ($n = 8$ mice per group). **f** Mouse weight was measured in each group at the indicated time intervals.

g Tumor growth inhibition in three BRAF^{V600E} CRC PDX models following with indicated treatments ($n = 5$ mice per group). **h** IHC of GPX4 and 4-HNE expressions in PDX model ($n = 5$). Data represent mean \pm SD, *** $P < 0.001$. Western-blot are representative of three independent experiments. Data were presented as mean \pm SD of three or five independent experiments (**a–d, h**). Data were analyzed by two-sided one-way ANOVA in (**e, h**). Source data are provided as a Source Data file.

PLK1 at the post-translational level. PLK1 translocates into the nucleus and phosphorylates Ser265 of CBX8, which is essential for CBX8 activation and the regulation of GPX4 expression. We also identified other phosphorylation sites on CBX8 based on BRAFi + EGFRi; however, the functions of these potential phosphorylation sites should be further investigated.

Unexpectedly, in this study, PLK1 could be activated and translocated into the nucleus after BRAFi \pm EGFRi treatment in BRAF^{V600E}

CRC. PLK1 kinases propagate pro-oncogenic activities through a network of transcription factors³⁰. However, the relationship between PLK1 and the MAPK pathway remains unclear. Several reports have suggested a relationship between the PLK1 and MAPK pathways. Upon recruitment to HER2, Shc1 facilitates the activation of the MAPK or PI3K pathways, and Shc1 can promote PLK1 activation by interacting with SHCBP1 in gastric cancer³¹. PLK1 promotes the development of Kras/Tp53-mutant lung adenocarcinoma through transcriptional

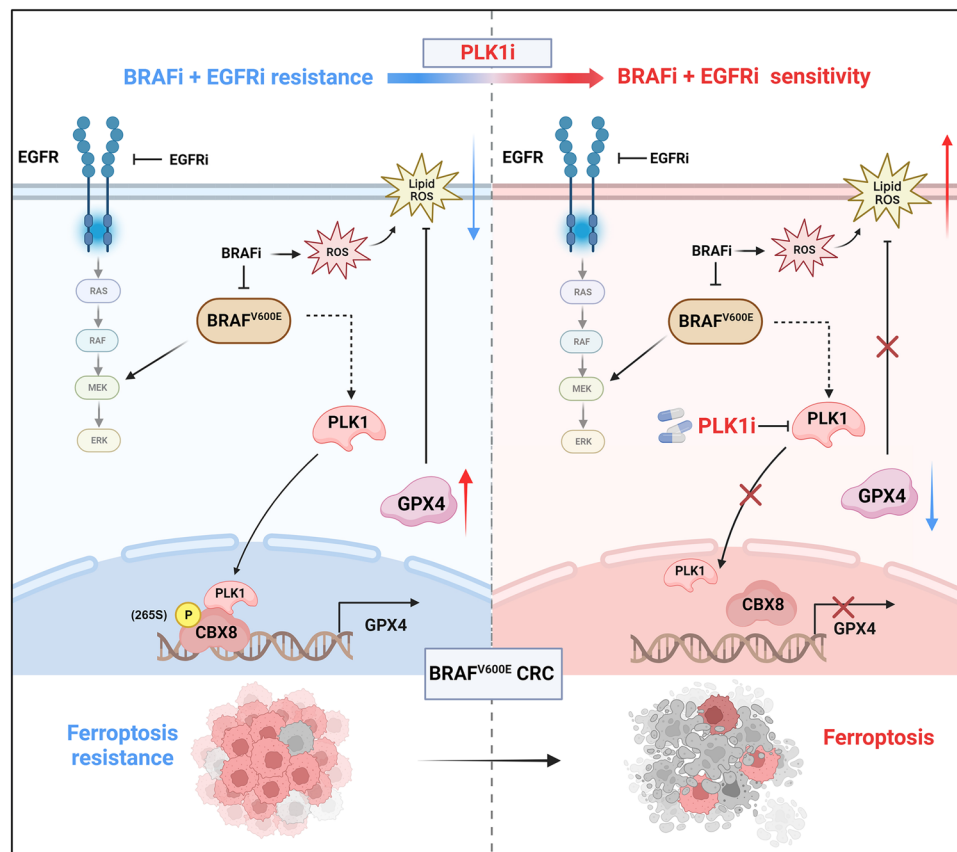


Fig. 8 | Schematic summary of the PLK1-CBX8-GPX4 axis in $BRAF^{V600E}$ CRC resistant to BRAFi ± EGFRi. $BRAF^{V600E}$ CRC develops resistance to EGFR and BRAF inhibitors via ferroptosis resistance. PLK1 inhibitors can block PLK1-CBX8 signaling

and suppress GPX4 transcription, thereby inducing ferroptosis and restoring sensitivity to BRAF and EGFR inhibitors.

activation of the RET receptor and MAPK signaling³². We reported that BRAF ± EGFR inhibition promoted feedback activation of PLK1 and demonstrated that the PLK1-CBX8-GPX4 axis was an important regulatory mechanism to prevent lipid peroxidation in $BRAF^{V600E}$ CRC resistant to BRAFi ± EGFRi treatment. Therefore, targeting the PLK1-CBX8-GPX4 axis triggers ferroptosis combined with BRAFi ± EGFRi in $BRAF^{V600E}$ CRC. However, further studies are required to reveal the exact mechanism by which BRAF-EGFR inhibition promotes the feedback activation of PLK1.

The production of a cellular ROS signature constitutes an opportunity to overcome resistance to BRAF ± EGFR inhibition in $BRAF^{V600E}$ CRC, and our preclinical results showed that PLK1 was a potential target for triplet combinations. Several inhibitors of PLK1 have been tested in clinical trials, such as BI2536, BI6727 (Vola), and NMS-1286937 (Onva), which are generally well-tolerated with a favorable pharmacokinetic profile, and clinical success is limited because of partial responses in patients with cancer³³. Therefore, clinical trials should focus on BRAF^{V600E} mCRC or evaluate these agents in combination with BRAF-targeted therapies. As there are no FDA-approved GPX4 inhibitors, PLK1 is an attractive drug target for clinical transformation. We showed that the addition of Onva to the current standard-of-care treatment, encorafenib (BRAF inhibitor) + cetuximab (EGFR inhibitor), resulted in sustainable and significant tumor growth inhibition with good drug tolerance in $BRAF^{V600E}$ CRC PDXs. In addition to safety, the FDA-approved PLK1is Onva and Vola could be rapidly translated to BRAF-targeted therapies in patients with $BRAF^{V600E}$ mCRC.

In conclusion, our results demonstrate that enhancement of GPX4 expression has a dominant role in mediating the resistance of $BRAF^{V600E}$ colorectal tumors to BRAF ± EGFR inhibitors. Moreover, the

synthetic lethal combination targeting GPX4 with BRAF ± EGFR uncovers the intrinsic susceptibility of $BRAF^{V600E}$ CRC to ferroptosis. We demonstrate that a PLK1-CBX8-GPX4 axis antagonizes the increasing cellular ROS production induced by BRAFi ± EGFRi and mediates $BRAF^{V600E}$ CRC resistant to BRAFi ± EGFRi. Targeting PLK1 with BRAF ± EGFR is a promising and clinical application treatment strategy to overcome drug resistance in $BRAF^{V600E}$ CRC.

Methods

Ethical statement

This research complies with all relevant ethical regulations. All animal experiments were conducted in accordance with the protocols approved by the Institutional Animal Care and Use Committee of the Jinan University. The experiment using patients' samples was approved by the Institutional Research Ethics Committee of Jinan University.

CRISPR screening

The HT-29 ($BRAF^{V600E}$ mutation) cells were transduced with a lentiviral human CRISPR knockout (hGeCKOv2) library (500× coverage) generated by the Zhang laboratory^{34,35} containing 122,411 sgRNAs targeting 19,050 protein-coding genes and 1864 miRNA precursors in the human genome. The cells were infected at a multiplicity of infection of 0.3 to ensure that most cells took up only one stable short guide RNA (sgRNA). Puromycin (10 µg/ml) was added to the cells 72 h after infection and maintained in the cultures for 3 days. After effective selection for puromycin resistance, we equally divided these HT-29 cells into four groups: the DMSO (day 0), DMSO (day 14), LGX818 (1 µM) treated for 14 days, or LGX818 (100 nM) + cetuximab (100 ng/ml) treated for 14 days groups. After drug selection, the cells were harvested, and genomic DNA was isolated using a DNA extraction kit

(Omega, D3396). The PCR products containing gRNA sequences that were integrated into the genomes of the cells were sequenced by parallel sequencing using a HiSeq 2000 (Illumina). Resistant genes were identified from sgRNA screen sequencing results using MAGeCK MLE analysis, as previously described³⁶. MAGeCK MLE calculates a “beta score” for each targeted gene to measure the degree of selection upon gene perturbation, similar to the “log fold-change” measurement in differential expression analysis. A positive beta score indicates that the gene is a positively screened gene, whereas a negative value indicates a negatively screened gene.

Patient sample collection

This study was approved by the Institutional Research Ethics Committee of Jinan University under the guidance of the Declaration of Helsinki (JNUKY-2023-0062). Written informed consent was obtained from participants, including consent to publish anonymized data, such as Sex, age and other clinical data. And The consent explicitly includes 1) Allow deidentified clinical data to be used for scientific research. 2) Allow aggregate data on demographic characteristics such as age and gender to be published in papers. A total 44 CRC samples with *BRAF*^{V600E} mutation were collected from January 2016 to November 2020 at the First Affiliated Hospital of Jinan University. All samples were confirmed to have *BRAF*^{V600E} mutation via NGS and taken from patients receiving standard guideline treatment. Another eight patients with *BRAF*^{V600E} CRC were treated using anti-BRAF + anti-EGFR, and samples were obtained before and after the anti-BRAF + anti-EGFR treatment. After obtaining the tissue samples during surgery, formalin fixation and paraffin embedding were performed using standard methods. Three fresh *BRAF*^{V600E} CRC tissue samples were collected for organoid culture and PDX model construction. Patients without detailed active follow-ups were excluded from this study. OS was defined as the time from the date of diagnosis to the date of either death from any cause or last follow-up. Informed consent was obtained from all the participants. As this is a retrospective analysis that does not involve additional patient participation, we obtained informed consent from patients but did not provide participant compensation for the retrospective data. We fully adhere to SAGER guidelines and our study design was not related to gender.

Cell lines, inhibitor, antibodies, and plasmids

Human CRC cell lines (Caco2, HT-29, Wdr, HCT-116, DLD1, Lovo, and RKO) were purchased from the American Type Culture Collection, and VAC0432 was purchased from BioVector NTCC Inc. The KM20 cells were purchased from BinSui Bio (Shanghai, China). All the cell lines were cultured according to the manufacturer's instructions. All the cells were cultured at 37 °C and 5% CO₂. All the cells were cultured in Dulbecco's modified Eagle's medium (DMEM) supplemented with 10% fetal bovine serum (FBS). Cell lines were passaged for no more than 6 months and were authenticated by STR analysis. No Mycoplasma infection was detected in any of the cell lines.

Encorafenib (LGX818) (T6487), cetuximab (T9905), Fer-1 (T6500), liproxstatin-1 (T2376), RSL3 (T3646), dabrafenib (T1903), vemurafenib (T2382), and gefitinib (T1181) were obtained from TargetMol. Onva (S7255) was purchased from Selleck. The antibodies used in western blotting, IF, and IHC staining are listed in Supplementary Data 10.

Construction of vectors and transfection

Flag-GPX4 and Flag-CBX8 expression plasmids or Flag-CBX8 with the indicated mutations was purchased or constructed from Sino Biological. For transient transfection, CRC cells were transfected with plasmids or siRNAs using Lipofectamine 3000 (Invitrogen), with vector plasmids serving as negative controls (NCs). The siRNAs were provided by OBiO Technology and GenePharma, and their sequences are listed in Supplementary Table 1. For stable transfection, CRC cells were infected with *GPX4* and *CBX8* overexpression plasmids or *CBX8*

and *PLK1* short hairpin RNA (shRNA) plasmids with lentivirus. The sequences of shRNA are listed in Supplementary Table 2. After screening with puromycin (10 µg/ml) for 3–5 days, the cells were harvested and used for subsequent experiments. For CRISPRi repression of *GPX4*, we constructed sgRNAs targeting the *GPX4* promoter sequence and the dCas9-KRAB-MeCP2 fusion protein using a lentivirus-based plasmid³⁷. Lentivirus-carrying gRNA or dCas9 was constructed and purchased from VectorBuilder, and the gRNA list is provided in Supplementary Table 3. Cells were infected with lentivirus-carrying dCas9-KRAB-MeCP2 for 48 h and selected by hygromycin (100 µg/ml). Subsequently, the cells that survived were infected with lentivirus-carrying non-sgRNA as NC or sgRNA targeting *GPX4* for 48 h and selected by puromycin (10 µg/ml). All sgRNA sequences are listed in Supplementary Table 3.

RNA isolation and real-time quantitative polymerase chain reaction

TRIzol reagent (Invitrogen) was used to extract total RNA from the cells and tissues. After reverse transcription was completed, the RNA expression levels were examined via quantitative polymerase chain reaction (qPCR) in triplicate on a Bio-Rad CFX96 using an SYBR Green kit (Takara, RR420A). The cDNA expression was normalized to that of glyceraldehyde 3-phosphate dehydrogenase or B-actin levels. Each qPCR was performed using three independent biological replicates. The primer sequences are listed in Supplementary Table 4.

Luciferase reporter assay

Cells were seeded into 24-well plates and transfected with luciferase reporter vectors, as described above. After 48 h, the cells were lysed and tested using a Dual-Luciferase Reporter Assay Kit (Promega, Madison, WI, USA) according to the manufacturer's instructions. Independent experiments were conducted in triplicates.

Western blotting analysis

Total protein was extracted using radioimmunoprecipitation assay lysis buffer containing a protease inhibitor cocktail. Protein concentrations were normalized using a BCA assay kit (Thermo Fisher Scientific, USA). Proteins from each group were loaded onto sodium dodecyl sulfate-polyacrylamide gel electrophoresis gels and separated before they were transferred to poly (vinylidene fluoride) (Millipore). The membranes were incubated with primary antibody against each target protein at 4 °C overnight. Subsequently, the membranes were incubated with the secondary antibody at 25 °C for 1 h. Immunoblots were developed using a chemiluminescent reagent (Beyotime, China) according to the manufacturer's instructions. The antibodies used are listed in Supplementary Data 8.

Coimmunoprecipitation assay

Cells were lysed in NETN buffer on ice for 30 min. Cell lysates were incubated with anti-Flag affinity gel for 2 h at 4 °C. Following precipitation, the pellets were washed four times with lysis buffer and then analyzed via immunoblotting.

Immunohistochemistry (IHC), immunofluorescence (IF), and hematoxylin–eosin (H&E) staining

Paraffin-embedded tissues were used for IHC staining, as previously described³⁸. According to the proportion of positive cells, none, 1–25%, 26–50%, 51–75%, and 76–100% were calculated as 0–4 points, respectively, and based on the dyeing intensity, the non, weak, medium, and strong were calculated as 0–3 points, respectively, and finally, the two parts were scored comprehensively. The median expression level was used to distinguish between the high- and low-expression groups. For IF, the harvested tissue from the colon was fixed in 4% paraformaldehyde, embedded, sectioned to obtain 4-µm sections, baked, and rehydrated. Subsequently, the section was retrieved using citric acid

buffer (pH, 6.0), permeabilized (0.1% Triton X-100/phosphate-buffered saline (PBS)), and blocked with QuickBlock™ Blocking Buffer for Immunol Staining (P0260, Beyotime, Biotechnology, China). Sections were incubated with primary antibodies at 4 °C overnight. The sections were washed thrice with PBS to remove nonspecific binding. The sections were then incubated with secondary antibodies at room temperature for 1 h. After incubation, the sections were then counterstained using 4',6-diamidino-2-phenylindole for 10 min and mounted in an antifade mounting medium (P0126, Beyotime, China). For hematoxylin and eosin staining, the sections were immersed in hematoxylin for 3 min, washed with water for 30 min, and stained with eosin for 3 min. The slides were covered with coverslips after dehydration in ethanol at different concentrations. The stained slides were imaged using an optical microscope (NIKON ECLIPSE 80i).

Cell viability and colony formation assays

Cell viability was assessed using the Cell Counting Kit-8 kit (ECK08, GLPBIO, CA, USA). Briefly, 5×10^3 cells were seeded into 96-well plates. The optical density (OD) value was measured at 450 nm using a microtiter plate reader. It is typically expressed as a percentage and calculated using the following formula: Inhibition ratio (%) = (vehicle group OD - treatment group OD)/vehicle group OD \times 100%. For the colony formation assays, 2×10^2 cells were seeded in 12-well plates. Different concentrations of drugs were added to specific wells to test cell sensitivity. The cell colonies were fixed with methanol and stained with 0.5% crystal violet before being photographed.

EdU cell proliferation assay

Organoids were seeded in 6-well plates and treated with LGX818, cetuximab, and Onva for 4 days. The pre-warmed EdU working solution (37 °C) was added to each well and further incubated for 2 h. The EdU stain procedure of organoids was referred to a previous study³⁹. Organoids were then placed under a fluorescence microscope for photographic analysis.

Propidium Iodide (PI) Staining

Cells were seeded in 6-well plates at a density of 1×10^6 cells/well and treated with the respective inhibitors for 48 h. For PI staining, 5 μ L of PI solution (1 mg/mL) was added to the cell suspension and incubated at room temperature for 15 min in the dark. DAPI was used to nucleus staining, and then placed under a fluorescence microscope for photographic analysis.

Cell cycle assay

The cells were seeded in 6-well plates and treated with the indicated drugs for 48 h. After sample preparation procedure, the cells were added using propidium iodide (PI) staining solution and 20 μ L RNase A solution (ERS0028, ELGBIO, China), and the cells were mixed and stained at room temperature for 30 min away from light. Flow cytometry was performed on a computer, and the number of events to be analyzed was $> 10,000$. The signal values included the following: FSC, SSC, PI-A, PI-H channel signals, and parallel period fitting analysis.

Malondialdehyde assay

The cells were collected, homogenized, and lysed. The protein concentration of each sample was determined using the Pierce™ BCA protein assay kit (23225, Thermo Fisher Scientific, USA). The samples were then assayed for lipid peroxidation levels using an MDA assay kit (S0131S; Beyotime Biotechnology, China) according to the manufacturer's instructions.

Glutathione assay

The total quantities of GSH were measured using a GSH Assay Kit (#BC1175, Solarbio) and normalized to the cell number according to the manufacturer's instructions.

Assessment of lipid peroxidation

The cells were dispensed in 6-well plates at a density of 6×10^5 cells/well. After treatment, the cells were incubated with Liperfluo (10 μ M) (L248, DOJINDO, Japan) for 1 h. The cells were then collected for analysis in a BD FACSCanto II flow cytometer. The excitation and emission wavelengths of the oxidized Liperfluo were 524 and 535 nm, respectively.

Iron assay

Intracellular chelatable iron was determined using the fluorescent indicator Phen Green™ SK (#P-14313) purchased from Thermo Fisher Scientific, the fluorescence of which was quenched by iron. For cells in vivo detection, 5 μ Mol/L Phen Green™ SK solution was used to incubate at 37 °C for 30 min. For organoids, 5 μ Mol/L Phen Green™ SK solution was used to incubate at 37 °C for 1 h.

Quantifying lipid peroxidation using BODIPY 581/591 C11

Lipid peroxidation was assessed using the lipid peroxidation probe C11 BODIPY 581/591 from MK Bio (MX5211). For detecting lipid peroxidation of Organoid, 10 μ M BODIPY 581/591 C11 working fluid Incubate at 37 °C for 1 h in the dark. Quantification was performed as follows: Oxidation was quantified as (green average intensity)/(red average intensity + green average intensity). Representative images were generated by merging red, green, and blue channels in ImageJ and adjusting the brightness/contrast for visualization (the same parameters applied to all images being compared to one another).

Liquid chromatography-mass spectrometry

In brief, tandem affinity purification in HT-29 cells expressing empty vector, FLAG-CBX8 was combined with anti-CBX8 antibody followed by the immunoprecipitation. Then add an appropriate amount of SDS-PAGE sample Buffer and heat at 95 °C for 10 min to release binding proteins. The protein samples were subjected to SDS-PAGE electrophoresis. The silver dye was used for color development and the target strip was cut for mass spectrometry analysis. Next, proteomic profiling was conducted by Shanghai LuMing Biotech (Shanghai, China). Lyophilized peptide mixtures were initially dissolved in aqueous solvent A (0.1% formic acid), followed by chromatographic separation on an Easy-NLC 1200 nano-HPLC platform. The separation utilized a dual-column configuration: 1) a 100 μ m \times 20 mm C18 trap column (Thermo Fisher Scientific) pre-equilibrated with solvent A, and 2) a 75 μ m \times 150 mm C18 analytical column (Thermo Fisher Scientific) operated at 300 nL/min. Following automated injection, peptides were retained on the trap column and subsequently transferred to the analytical column. A binary gradient was applied for elution, with solvent B comprising 0.1% formic acid in acetonitrile. To minimize background interference, the system underwent a 30-minute equilibration cycle with a blank solvent prior to sample runs. Finally, separated peptides were subjected to electrospray ionization and detected using a Q-Exactive Orbitrap mass spectrometer (Thermo Fisher Scientific). Mass spectrometric analysis was conducted with instrumental calibration performed using a standard solution across the m/z range of 300–1600. Data acquisition employed a data-dependent (DDA) mode, wherein each full MS scan (MS1) at 45,000 resolution (at m/z 200) triggered the selection of the 20 most abundant precursor ions for subsequent MS/MS analysis. High-energy collision-induced dissociation (HCD) was applied with 28% normalized collision energy (NCE), utilizing a 25-s dynamic exclusion window to minimize redundant fragmentation. Detection parameters were configured as follows: MS1 scans operated with an automatic gain control (AGC) target of 1×10^6 and 50 ms maximum injection time, while MS2 scans attained 15,000 resolution with AGC target 1×10^5 under identical injection duration. Raw spectra were processed via MaxQuant (v2.1.0) against the UniProt *Mus musculus* database, incorporating fixed carbamidomethylation (C), variable modifications of methionine oxidation and

N-terminal acetylation, tryptic digestion allowance for ≤ 2 missed cleavages, and mass tolerances of 20 ppm (first search) and 4.5 ppm (main search).

Chromatin immunoprecipitation quantitative polymerase chain reaction (ChIP-qPCR)

HEK-293T cells transfected with plasmids were fixed with 1% formaldehyde and cross-linking was quenched with glycine. The cells were washed with PBS, scraped in cold ChIP buffer (PBS + PIC) and centrifuged. The pellet was then digested at 37 °C in ChIP lysis buffer (Buffer B, 1 M DTT, Micrococcal Nuclease, 0.5 M EDTA). After centrifugation, the cells were sonicated in ChIP Buffer (containing PIC), and the supernatant was collected as the crosslinked chromatin preparation. Four volume of ChIP dilution buffer (ChIP Buffer, PIC) was added to the supernatant, and 10 μ L of the mixture was taken out as 2% Input. The remaining diluted chromatin was incubated with CBX8 antibody and Normal Rabbit IgG (as the negative control), respectively overnight at 4 °C with rotation. Protein G Magnetic Beads were added and incubated for 2 h at 4 °C. The magnetic beads were washed three times with low salt solution (ChIP Buffer) and once with high salt solution (ChIP Buffer, 5 M NaCl). The magnetic beads and 2% Input were resuspended in ChIP elution buffer (ChIP Elution Buffer), and 5 M NaCl and Proteinase K were added, followed by incubation at 65 °C overnight. The DNA was purified using a spin column and then detected by qPCR assays with custom primers. The qPCR primers were designed as follows: Fwd: AATCCAAACCCCTGCCTGT, Rev: CCATACTGCCCCACATCTTG.

Animal experiments

All animal procedures were approved by the Institutional Animal Care and Use Committee of the Jinan University (approval number: 20210708-03). Four-week-old female nude BALB/c or NDG mice were purchased from BesTest (Zhuohai, China) and were randomly assigned to experimental groups and maintained under controlled environmental conditions (temperature: 22–24 °C; relative humidity: 40–70%) with a standardized 12-hour light/dark cycle. All animals had ad libitum access to autoclaved food and water throughout the study period. HT-29 or WiDr cells (5×10^6 cells) mixed with PBS (200 μ L/each mouse) was subcutaneously injected into the fat pads of mice. After a tumor grew to 100 mm³, the mice were randomized into different groups, and they were treated with vehicle (0.2% Tween 80 and 1% methylcellulose in sterile PBS by daily gavage); BRAFi: LGX818 (30 mg kg⁻¹, by mouth daily); BRAFi + EGFRi: LGX818 (10 mg kg⁻¹, by mouth daily) + cetuximab (10 mg/kg, intraperitoneally daily); RSL3 (10 mg kg⁻¹, intraperitoneally daily); Onva (10 mg kg⁻¹, by mouth daily); or Fer-1 (10 mg kg⁻¹, intraperitoneally daily). The subcutaneous tumor maximum volume was 2000 mm³ and authorized by the Committees on Animal Research and Ethics, and was not exceeded at any time during the experiments. The tumor volume was measured every 3 days, and the volume was estimated according to the following formula: volume = length \times width²/2. The mice were sacrificed at the end of the experiment, and the xenografts were resected, weighed, and photographed.

PDX experiments

Fresh patient samples were obtained from the Department of General Surgery at the First Affiliated Hospital of Jinan University. All samples were collected after obtaining written informed consent from the patients. Moreover, the BRAF^{V600E} mutation was confirmed using NGS. We selected three cases with BRAF^{V600E} mutation for the PDX experiment. Patient-derived tumor fragments (2–3 mm³) were surgically xenografted under the skin of 6-week-old male NCG mice. When the tumors reached approximately 100 mm³, the mice received an intraperitoneal injection of the indicated treatment and NC or CBX8, PLK1 siRNA in vivo. SiRNA (5 nmol/20 g, RiboBio, Guangzhou, China) against CBX8 or PLK1 was performed via intraperitoneal injection every 3 days.

Proteomic and phosphoproteomic analyses

The four-dimensional (4D) label-free quantification (LFQ) technology was used to perform proteomics and phosphoproteomics analyses. The HT-29 cells were treated with DMSO (NC), LGX818 (1 μ M), or LGX818 (100 nM) + Cet (100 ng/ml) for 48 h. Proteomic analysis was performed at the Jingjie PTM BioLab Co. Ltd. (Hangzhou, China) Proteomics Facility. For protein quantification and criteria for protein identification, the secondary mass spectrum data from this experiment were retrieved using MaxQuant (version 1.6.15.0). Regarding the setting of retrieval parameters, the Homo_sapiens_9606_SP_20201214.fasta (20395 sequences) database was used. The false discovery rate for protein and peptide spectrum matching identification was set at 1%.

Bioinformatics analysis was performed, as previously described⁴⁰. Differential analysis was performed, with a threshold for significant upregulation set at a fold change > 1.5 and a threshold for significant downregulation set at a fold change of <1/1.5. Briefly, Gene Ontology and KEGG functional enrichment analyses were performed using InterProScan ($P < 0.05$) and the KOG database (<http://www.ncbi.nlm.nih.gov/KOG>). The sequence model, with amino acids at specific modification positions, was analyzed using MoMo (motif-x algorithm)⁴¹.

Patient-derived organoid

CRC organoids were established, as previously described⁴². Fresh BRAF^{V600E} mutation CRC tissues were cut into pieces, washed with ice-cold PBS, and then digested with ethylenediamine tetraacetic acid and 0.5 mM dithiothreitol for 1 h. After centrifugation at 300 g for 5 min, the tissue fragments were digested in a digestion solution composed of advanced DMEM/F-12 (Gibco), 1 mg/ml collagenase type I (Worthington), 50 U/ml hyaluronidase (Worthington), and 125 μ g/ml Dispase II (Gibco) at 37 °C for 30 min, filtered through a 70- μ m cell strainer, and centrifuged at 300 g for 5 min. Subsequently, the pellet was embedded in Matrigel until solidification and cultured in a medium composed of advanced DMEM/F-12, 5% FBS, 1% penicillin–streptomycin, 1 \times GlutaMax supplement (Gibco), and 10 mM HEPES (Gibco), and the culture was started. When organoids were formed, they were separated into original medium into different groups. After the indicated treatment for 4 days, organoids were imaged and the sizes were measured using Image J.

Statistics and reproducibility

All experiments were performed at least thrice, and IF staining, IHC staining, TEM, and western blot assay representative images are shown. Data were analyzed using GraphPad Prism 9.5.1 (GraphPad Software). The unpaired Student's t-test was used to analyze the differences between the two groups. Log- or square-root transformation or nonparametric testing was used if the data were not normally distributed. Differences among the three groups were evaluated using One-way ANOVA analysis of variance followed by Tukey's post-hoc test. Survival curves were described using Kaplan–Meier plots and compared using the log-rank test. The results are presented as means \pm standard deviation. $P < 0.05$ was considered statistically significant.

Reporting summary

Further information on research design is available in the Nature Portfolio Reporting Summary linked to this article.

Data availability

All data generated or analyzed during this study are included within the article, Supplementary Information, the Source Data file, and the protein mass spectrometry raw data are available through the ProteomeXchange Consortium (<http://www.proteomexchange.org/>) via the PRIDE partner repository with dataset identifiers PXD058218. The CRISPR Screen sequencing data has been deposited in the GEO database: (<https://www.>

ncbi.nlm.nih.gov/geo/query/acc.cgi?acc=GSE283185). And the immuno precipitation-Mass spectrometry data is available at the PRIDE dataset with dataset identifiers IPX0010313000 (<https://www.iprox.cn/page/home.html>). Source data are provided with this paper.

References

- Siegel, R. L., Wagle, N. S., Cercek, A., Smith, R. A. & Jemal, A. Colorectal cancer statistics, 2023. *CA Cancer J. Clin.* **73**, 233–254 (2023).
- Sahin, I. H. & Klostergaard, J. BRAF Mutations as Actionable Targets: A Paradigm Shift in the Management of Colorectal Cancer and Novel Avenues. *JCO Oncol. Pract.* **17**, 723–730 (2021).
- Ciombor, K. K., Strickler, J. H., Bekaii-Saab, T. S. & Yaeger, R. BRAF-Mutated Advanced Colorectal Cancer: A Rapidly Changing Therapeutic Landscape. *J. Clin. Oncol.* **40**, 2706–2715 (2022).
- Caputo, F. et al. BRAF-Mutated Colorectal Cancer: Clinical and Molecular Insights. *Int J. Mol. Sci.* **20**, 5369 (2019).
- Pan, J. H. et al. Development of small-molecule therapeutics and strategies for targeting RAF kinase in BRAF-mutant colorectal cancer. *Cancer Manag Res* **10**, 2289–2301 (2018).
- Seligmann, J. F. et al. Investigating the poor outcomes of BRAF-mutant advanced colorectal cancer: analysis from 2530 patients in randomised clinical trials. *Ann. Oncol.: Off. J. Eur. Soc. Med. Oncol.* **28**, 562–568 (2017).
- Oddo, D. et al. Molecular Landscape of Acquired Resistance to Targeted Therapy Combinations in BRAF-Mutant Colorectal Cancer. *Cancer Res.* **76**, 4504–4515 (2016).
- Huijberts, S. C., van Geel, R. M., Bernards, R., Beijnen, J. H. & Steeghs, N. Encorafenib, binimetinib and cetuximab combined therapy for patients with BRAFV600E mutant metastatic colorectal cancer. *Future Oncol. (Lond., Engl.)* **16**, 161–173 (2020).
- Kopetz, S. et al. Phase II Pilot Study of Vemurafenib in Patients With Metastatic BRAF-Mutated Colorectal Cancer. *J. Clin. Oncol.* **33**, 4032–4038 (2015).
- Janku, F. Advances on the BRAF Front in Colorectal Cancer. *Cancer Discov.* **8**, 389–391 (2018).
- van Geel, R. et al. A Phase Ib Dose-Escalation Study of Encorafenib and Cetuximab with or without Alpelisib in Metastatic BRAF-Mutant Colorectal Cancer. *Cancer Discov.* **7**, 610–619 (2017).
- Corcoran, R. B. et al. Combined BRAF, EGFR, and MEK Inhibition in Patients with BRAF(V600E)-Mutant Colorectal Cancer. *Cancer Discov.* **8**, 428–443 (2018).
- Kopetz, S. et al. Encorafenib, Binimetinib, and Cetuximab in BRAF V600E-Mutated Colorectal Cancer. *N. Engl. J. Med.* **381**, 1632–1643 (2019).
- Morris, V. K. & Bekaii-Saab, T. Improvements in Clinical Outcomes for BRAF(V600E) -Mutant Metastatic Colorectal Cancer. *Clin. Cancer Res* **26**, 4435–4441 (2020).
- Prahalad, A. et al. Unresponsiveness of colon cancer to BRAF(V600E) inhibition through feedback activation of EGFR. *Nature* **483**, 100–103 (2012).
- Cesi, G., Walbrecht, G., Zimmer, A., Kreis, S. & Haan, C. ROS production induced by BRAF inhibitor treatment rewires metabolic processes affecting cell growth of melanoma cells. *Mol. Cancer* **16**, 102 (2017).
- Lee, J. & Roh, J. L. Targeting GPX4 in human cancer: Implications of ferroptosis induction for tackling cancer resilience. *Cancer Lett.* **559**, 216119 (2023).
- Tang, B. et al. CBX8 exhibits oncogenic properties and serves as a prognostic factor in hepatocellular carcinoma. *Cell Death Dis.* **10**, 52 (2019).
- Kumar, S., Sharma, A. R., Sharma, G., Chakraborty, C. & Kim, J. PLK-1: Angel or devil for cell cycle progression. *Biochim. et. biophys. acta* **1865**, 190–203 (2016).
- Francescangeli, F. et al. Proliferation state and polo-like kinase1 dependence of tumorigenic colon cancer cells. *Stem cells (Dayt., Ohio)* **30**, 1819–1830 (2012).
- Zhang, J., Zhang, L., Wang, J., Ouyang, L. & Wang, Y. Polo-like Kinase 1 Inhibitors in Human Cancer Therapy: Development and Therapeutic Potential. *J. Med. Chem.* **65**, 10133–10160 (2022).
- Chiappa, M. et al. Present and Future Perspective on PLK1 Inhibition in Cancer Treatment. *Front Oncol.* **12**, 903016 (2022).
- Wang, Z. et al. Cetuximab and vemurafenib plus FOLFIRI (5-fluorouracil/leucovorin/irinotecan) for BRAF V600E-mutated advanced colorectal cancer (IMPROVEMENT): An open-label, single-arm, phase II trial. *Eur. J. Cancer* **163**, 152–162 (2022).
- Tan, L. et al. A Phase Ib/II Trial of Combined BRAF and EGFR Inhibition in BRAF V600E Positive Metastatic Colorectal Cancer and Other Cancers: The EVICT (Erlotinib and Vemurafenib In Combination Trial) Study. *Clin. Cancer Res.* **29**, 1017–1030 (2023).
- Viswanathan, V. S. et al. Dependency of a therapy-resistant state of cancer cells on a lipid peroxidase pathway. *Nature* **547**, 453–457 (2017).
- Yagoda, N. et al. RAS-RAF-MEK-dependent oxidative cell death involving voltage-dependent anion channels. *Nature* **447**, 864–868 (2007).
- Li, F. J. et al. System X(c) (-)/GSH/GPX4 axis: An important antioxidant system for the ferroptosis in drug-resistant solid tumor therapy. *Front Pharm.* **13**, 910292 (2022).
- Ng, L. et al. High Expression of a Cancer Stemness-Related Gene, Chromobox 8 (CBX8), in Normal Tissue Adjacent to the Tumor (NAT) Is Associated with Poor Prognosis of Colorectal Cancer Patients. *Cells* **11**, 1852 (2022).
- Choi, B. H., Colon, T. M., Lee, E., Kou, Z. & Dai, W. CBX8 interacts with chromatin PTEN and is involved in regulating mitotic progression. *Cell Prolif.* **54**, e13110 (2021).
- Iliaki, S., Beyaert, R. & Afonina, I. S. Polo-like kinase 1 (PLK1) signaling in cancer and beyond. *Biochem Pharm.* **193**, 114747 (2021).
- Shi, W. et al. Hyperactivation of HER2-SHCBP1-PLK1 axis promotes tumor cell mitosis and impairs trastuzumab sensitivity to gastric cancer. *Nat. Commun.* **12**, 2812 (2021).
- Kong, Y. et al. The kinase PLK1 promotes the development of Kras/Tp53-mutant lung adenocarcinoma through transcriptional activation of the receptor RET. *Sci. Signal.* **15**, eabj4009 (2022).
- Su, S., Chhabra, G., Singh, C. K., Ndiaye, M. A. & Ahmad, N. PLK1 inhibition-based combination therapies for cancer management. *Transl. Oncol.* **16**, 101332 (2022).
- Shalem, O. et al. Genome-scale CRISPR-Cas9 knockout screening in human cells. *Science* **343**, 84–87 (2014).
- Sanjana, N. E., Shalem, O. & Zhang, F. Improved vectors and genome-wide libraries for CRISPR screening. *Nat. methods* **11**, 783–784 (2014).
- Wang, B. et al. Integrative analysis of pooled CRISPR genetic screens using MAGeCKFlute. *Nat. Protoc.* **14**, 756–780 (2019).
- Yeo, N. C. et al. An enhanced CRISPR repressor for targeted mammalian gene regulation. *Nat. methods* **15**, 611–616 (2018).
- Yang, Y. et al. Targeting LAYN inhibits colorectal cancer metastasis and tumor-associated macrophage infiltration induced by hyaluronan oligosaccharides. *Matrix Biol.: J. Int. Soc. Matrix Biol.* **117**, 15–30 (2023).
- O'Rourke, K. P., Dow, L. E. & Lowe, S. W. Immunofluorescent Staining of Mouse Intestinal Stem Cells. *Bio-Protoc.* **6**, e1732 (2016).
- Li, Q. et al. Dihydroartemisinin regulates immune cell heterogeneity by triggering a cascade reaction of CDK and MAPK phosphorylation. *Signal Transduct. Target. Ther.* **7**, 222 (2022).

41. Cheng, A., Grant, C. E., Noble, W. S. & Bailey, T. L. MoMo: discovery of statistically significant post-translational modification motifs. *Bioinformatics* **35**, 2774–2782 (2019).
42. Amodio, V. et al. EGFR Blockade Reverts Resistance to KRAS(G12C) Inhibition in Colorectal Cancer. *Cancer Discov.* **10**, 1129–1139 (2020).

Acknowledgements

This research was supported by the Guangzhou Basic and Applied Basic Research Foundation (2024A1515030010; 2022A1515011695; 2020A1515110049; SL2023A04J01099), the Science and Technology Project of Guangdong Province (2023A0505050149 TL), the National Natural Science Foundation of China (82204436; 82002491), the project of Guangzhou science and technology plan (2022010200084; 2022010200065), Major Talent Program of Guangdong Provincial (2019QN01Y933 TL), Hunan Provincial Natural Science Foundation (2023JJ50067) and Scientific Research Fund of Hunan Provincial Education Department (21B0749).

Author contributions

Z Zhao, J He and S Qiu: conduction of experiments, acquisition of data, analysis of experimental data and drafted the manuscript. L Wang and S Huangfu: Investigation, visualization and methodology. Y Hu, Q Wu and Y Yang: data curation, software and formal analysis. X Li and M Huang: technical expertise in experimental design and manuscript editing. G Xiao: in charge of chromatin immunoprecipitation (ChIP) assay and dual-Luciferase reporter assay during the revision process. S Liu, H Guan, Z Chen and X Zhang: assay optimization, acquisition, and analysis and interpretation of histology and pathology. Y Zhang, H Ding, X Zhao and Y Pan: conduct of experiments and acquisition of clinical data. T Liu and YP Wu: provided technical expertise in experimental design and manuscript editing. J Pan: funding acquisition, designed the study and writing-review and editing the draft.

Competing interests

The authors declare no competing interests.

Additional information

Supplementary information The online version contains supplementary material available at <https://doi.org/10.1038/s41467-025-58992-z>.

Correspondence and requests for materials should be addressed to Tongzheng Liu, Yanping Wu or Jinghua Pan.

Peer review information *Nature Communications* thanks the anonymous reviewer(s) for their contribution to the peer review of this work. A peer review file is available.

Reprints and permissions information is available at <http://www.nature.com/reprints>

Publisher's note Springer Nature remains neutral with regard to jurisdictional claims in published maps and institutional affiliations.

Open Access This article is licensed under a Creative Commons Attribution-NonCommercial-NoDerivatives 4.0 International License, which permits any non-commercial use, sharing, distribution and reproduction in any medium or format, as long as you give appropriate credit to the original author(s) and the source, provide a link to the Creative Commons licence, and indicate if you modified the licensed material. You do not have permission under this licence to share adapted material derived from this article or parts of it. The images or other third party material in this article are included in the article's Creative Commons licence, unless indicated otherwise in a credit line to the material. If material is not included in the article's Creative Commons licence and your intended use is not permitted by statutory regulation or exceeds the permitted use, you will need to obtain permission directly from the copyright holder. To view a copy of this licence, visit <http://creativecommons.org/licenses/by-nc-nd/4.0/>.

© The Author(s) 2025